UC Riverside

UC Riverside Electronic Theses and Dissertations

Title

Superconducting Magnetometers and Electronic Control System

Permalink

https://escholarship.org/uc/item/0c8732g8

Author

Zhou, Yuchao

Publication Date

2020

Copyright Information

Peer reviewed|Thesis/dissertation

UNIVERSITY OF CALIFORNIA
RIVERSIDE

Superconducting Magnetometers and Electronic Control System

A Dissertation submitted in partial satisfaction
of the requirements for the degree of

Doctor of Philosophy

in

Electrical Engineering

by

Yuchao Zhou

September 2020

Dissertation Committee:

Dr. Shane Cybart, Chairperson
Dr. Walid Najjar
Dr. Shaolei Ren

The Dissertation of Yuchao Zhou is approved:

_____

_____

_____

Committee Chairperson

University of California, Riverside

Acknowledgments

First and foremost, I would like to gratefully thank my advisor Professor Shane A. Cybart. We have known each other and have been working together for more than seven years, ever since I was an undergraduate student at UC San Diego. Thank you for grabbing me and letting me pursue the study as a graduate student. I would also like to thank my post doc, Ethan. You are the one who brought me into the field and taught me the majority of the knowledge and skills of superconductors starting from back when we were both in San Diego. I really enjoyed the late nights when we did the measurements together. There is another professor I would like to mention from the previous lab, Bob Dynes. Thank you for all the helpful discussions and advice. These conversations involving both scientific research and normal life have benefited me a lot. It is my honor to meet you all in San Diego and it has definitely changed my life.

To my other post doc Hao, you are such a knowledgeable and hard-working guy. Thank you for all the helpful discussions and for the help in writing some of my chips. I wish for you to have a wonderful professorship at Kansas. Special thanks to my first labmate in Riverside, Stephen McCoy. You opened my mind to many different fields and taught me a lot through the real life stories you had. I apologize for being mean to you when we first met. I would also like to thank my other labmates, Jay, Anthony, Yan-Ting, and Han, whom I have been working with for 4 years. You are all great people to work with and collaborate with together. I appreciate all the help you have given to me. Special thanks to Miranda as well. Thank you for helping me to improve my technical writing skills and for checking the grammar of my broken English. I would like to thank Guy Covert from

Cryogenic Control Systems, Inc. Thank you for all the suggestions on the digital flux locked loop.

Finally, I thank those people who love me and whom I love. My girlfriend, you are the moon to my dark sky. Thank you grandma Kay, I actually never used you as an excuse for school, believe it or not. Thanks to my roommate Nick and my cute little girl, Mila. I am very lucky to meet you and to live with you. At last, I would like to thank my parents, for giving me strength to chase my illusory dream.

To my parents for all the support. Also to my crazy, fragile heart that has

supported me for so long.

ABSTRACT OF THE DISSERTATION

Superconducting Magnetometers and Electronic Control System

by

Yuchao Zhou

Doctor of Philosophy, Graduate Program in Electrical Engineering
University of California, Riverside, September 2020
Dr. Shane Cybart, Chairperson

Superconducting devices provide unique properties and new potential for future electronics. Magnetometers and gradiometers based on superconducting materials such as Superconducting Quantum Interference Devices (SQUIDs) are amongst the most sensitive detectors of magnetic field [1]. They have been widely used in geological, biomedical, and electromagnetic analysis [1–15]. More and more, applications require superconductor sensors with large dynamic ranges and high slew-rates. Additionally, the capability of parallel processing many sensors in high demand. This dissertation reports on the experimental results of several high temperature superconductor based magnetometers and the further analysis of their electronic properties, followed by a novel approach using high-speed digital electronics to control some of the sensors.

Currently, commercialized control systems based on analog flux-locked loops (FLL) are mainly designed for low-transition temperature SQUIDs. Distinct analog circuits have to be designed or customized to each type of SQUID sensor with different electrical properties for optimal performance. The rapid advancement in the performance of high-frequency

digital components, driven by the mobile communication industry, motivates the further development of digital FLL (DFLL). In order to develop a system with adjustable features for different types of SQUIDs, we used Field Programmable Gate Arrays (FPGA) to implement the new DFLL. This approach can be easily scaled up to support a large number of sensors instead of having multiple analog circuits. The reprogrammable feature of the FPGA gives the system the capability to modify the FLL for SQUID sensors in real time. The system combines both traditional FLL with flux jump and counting together to provide a much larger dynamic range. At the same time, algorithms have been developed for analyzing and tracking in order to achieve an accurate lock on both SQUIDs. This approach is also a potential electronics system that can operate other magnetometers such as long junctions. Additional digital signal processing (DSP) can be used for SQUID data analysis, including parallel processing, digital gradiometer subtraction, and SQUID imaging.

Contents

List of Figures

Chapter 1

Introduction

1.1 YBCO

The most commonly studied high-temperature superconducting (HTS) material is $YBa_2Cu_3O_{7-\delta}$ (YBCO) [22] because of its high transition temperature (high-T_C) and critical current density. Like many of the HTS materials, it is a cuprate that crystallizes in a complex orthorhombic unit cell structure, Fig. 1.1 [23]. As a result, electrical transport in the material is highly anisotropic in all 3 lattice directions. The resistivity along c-axis is much bigger than the resistivity along the b-axis or a-axis, where $\rho_c > 3\rho_b$ and $\rho_a \approx 3\rho_b$. It is extremely difficult to grow practical multilayer YBCO junctions. Additional problems arise because of its highly anisotropic superconducting coherence length and penetration depth.

Along the b-axis, chains of copper and oxygen atoms create the preferred path of conduction. The binding of the oxygen atom in this chain has a low activation energy of
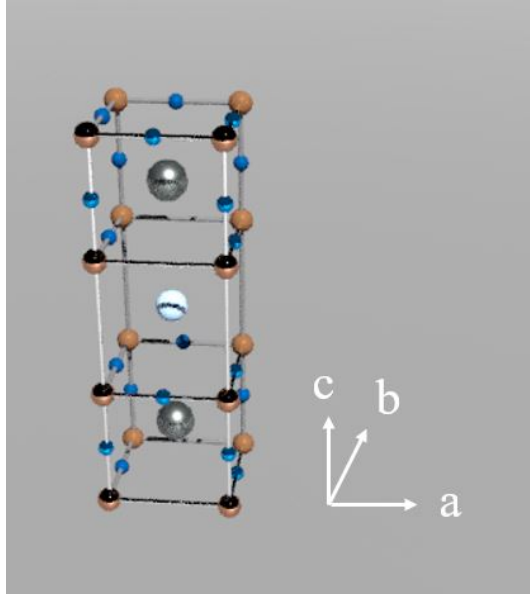
Figure 1.1: Orthorhombic crystal structure of YBCO superconducting coherence length in a-b plane $\approx$ 2 nm and along c axis $\approx$ 0.2 nm. The penetration depth in a-b plane is about 150 nm and about 800 nm along c axis [16].

1 eV and can be easily moved to an interstitial site. This result in a degradation of the superconducting properties and, in extreme cases, completely destroys superconductivity and metallic behavior.

However, YBCO is still a promising material for a variety of superconducting applications. Low transition temperature superconductors (LTS) like Niobium, operate at liquid helium temperatures of ($\sim$4 K). After the discovery of high transition temperature superconductor (HTS) ceramic materials, much research has been done to fabricate HTS devices. The operation temperature ($\sim$80 K) of the HTS ceramic materials could significantly decrease the complexity, cost, power and weight of the sensors themselves and the associated refrigeration system.

1.2 Ion irradiation

One of the major advancements in the facile processing of HTS devices is the use of ion irradiation. This was first developed in Bell Labs in 1987 [17,24]. Their researches shows that an increase of fluences of ion implementation reduces the critical current density in YBCO, Fig.1.2. Because of the material's sensitivity to defects, ion irradiation can be used to modify the YBCO, analogous to transiting from superconductor to non-superconductor and increasing the resistance of the material by photolithography. Specifically, by increasing the doses of irradiation, conductivity and T_C in the film decrease in a controlled way. This is accompanied by an exponential decrease in the critical current density. For moderate doses of irradiation, the YBCO thin film is completely converted from a superconductor to an insulator, Fig. 1.3
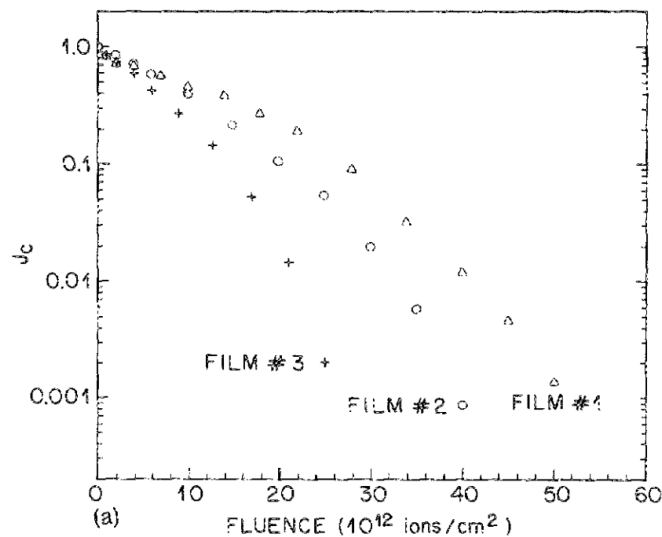
Figure 1.2: Reduction of Jc in three different YBCO films with respect to different doses of 1 MeV Ne$^+$ ion beam [17]

3
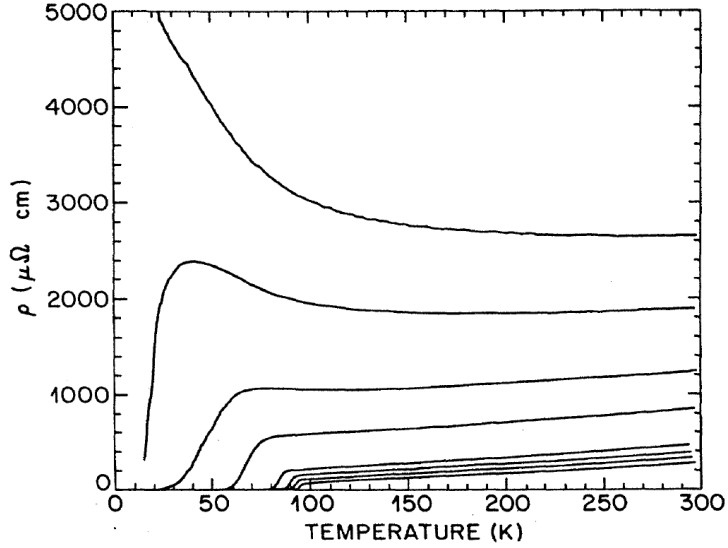
Figure 1.3: Resistivity change of YBCO film with time after irradiated by 1 MeV Ne$^+$ ions at fuences of (0, 0.1, 2.5, 4.0, 10.0, 15.0, 20.0, and 22.0) $\times 10^{13}$ ions/cm^2 [17].

1.3 Focused Ion Beam

A novel way to irradiate the surface of thin films from superconducting to insulating developed in 2006 with the invention of the helium ion microscope [25]. This process is highly controllable, with a minimum beam size of 0.5 nm, decreasing the disorder region of YBCO to the nano scale. On this scale, it is now possible to create smaller and more uniform barriers on thin film YBCO more accessibly than ever [26]. Along with this technology, studies about HTS Josephson junctions can be fabricated on a nano scale with similar tunneling lengths to LTS.

1.4 Josephson Junctions

The most important superconducting device is the Josephson Junction, first predicted by Brain Josephson in 1962 Fig. 1.4. A Josephson Junction is basically composed of

two pieces of superconductors separated by a thin metallic or insulating barrier, Fig. 1.4.

A Josephson Junction is the fundamental component of most superconducting devices.
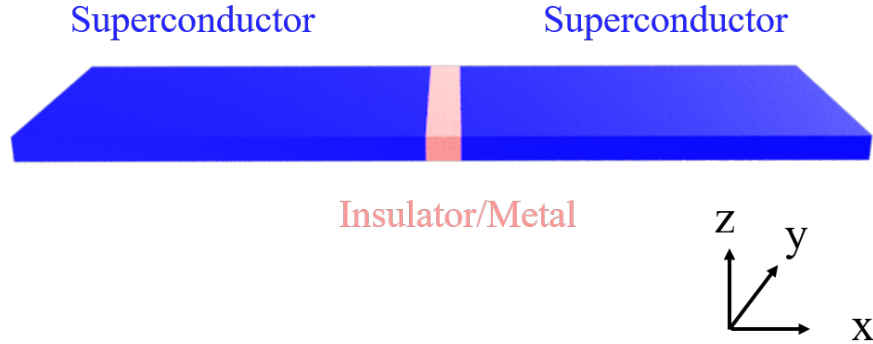
Figure 1.4: A schematic of Josephson Junctions. Current flows in y direction

By separating the superconductor into two pieces using a barrier, a phase difference is created between the wave function of the two superconductors on each side, often known as Josephson Phase (φ). This phase difference will drive the Cooper pairs to quantum tunnel through the barrier and form a supercurrent going through the weak junction without any potential voltage [27]. This phase coupling of the Josephson junction is strongly correlated to the barrier width. Using the FHB technology, which allows for pattern control on the nanoscale, it is now possible to improve the junction performance with these devices. The equation below describes the relationship between the current flowing through the junction and the Josephson phase.

$$I_S = I_C \sin \varphi \tag{1.1}$$

The critical current, I_C, is the maximum current that can go through the junction with zero voltage. This equation is also known as the first Josephson equation [28]. After applying potential voltage, the phase difference along x-axis changes with time and drives more current through the junction [27].

$$V = \frac{d\varphi}{dt}\frac{h}{2e} \tag{1.2}$$

This equation is also known as the second Josephson equation. It describes the relationship between the voltage across the junction with respect to the time dependent phase change.

1.4.1 RCSJ model

The Junction itself can be modeled as the ideal junction in parallel with a resistor and a capacitor, Fig. 1.5. This model was developed in 1968 by Stewart [29] and McCumber [30] and was well known as resistively capacitive shunted junction (RCSJ) model.
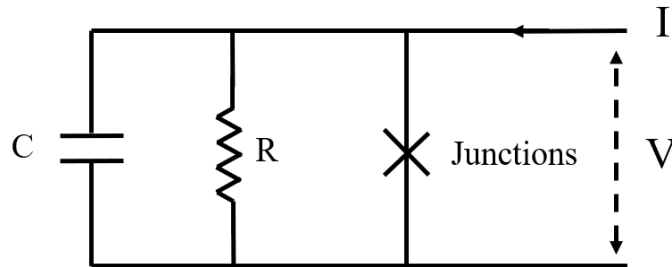
Figure 1.5: RCSJ circuit model

Based on the model, the relationship between the voltage and the current is:

$$I = I_c \sin \varphi + \frac{V}{R_N} + C\frac{dV}{dt} \tag{1.3}$$

Due to the small width of the junction barrier, the capacitance of the Josephson junction is usually small and can be ignored in the RCSJ model. After applying the phase change with respect to time on the applied voltage, the current becomes:

$$I = I_C \sin(\varphi) + \frac{d\varphi}{dt}\frac{h}{2eR_N} \tag{1.4}$$

It shows that when current is smaller than the critical current I_C voltage is equal to zero. When current is bigger than I_C, the voltage becomes:

$$V = I_C R_N \sqrt{(\frac{I}{I_C})^2 - 1} \tag{1.5}$$

The I-V characteristic is shown in Fig. 1.6.
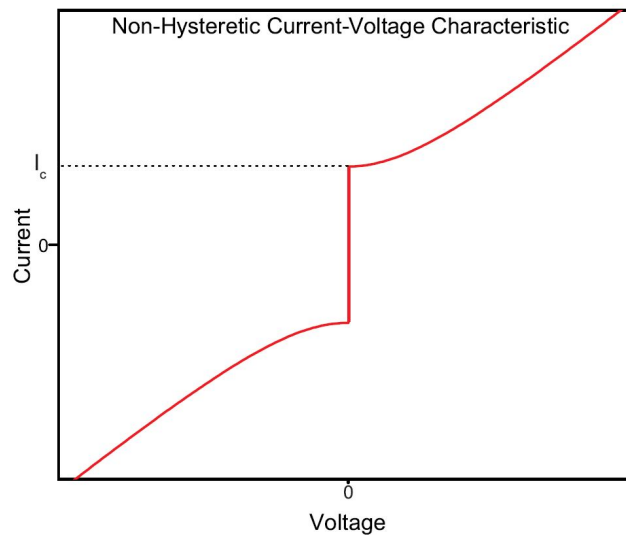
Figure 1.6: I-V characteristic for Josephson junction

7

1.4.2 Magnetic Field

By putting a Josephson junction into an external magnetic field towards the z-axis, the phase varies along the y-axis and causes current density changes along the junction

$$\frac{d\varphi}{dy} = \frac{-2et}{\hbar}B = \frac{2\pi\Phi}{\Phi_0} \tag{1.6}$$

where t is the effective barrier thickness. With a constant external field, this can be integrated and inserted into the first Josephson Junction equation 1.7 obtain:

$$I_S(\Phi) = I_C(0)\left|\frac{\sin\pi\frac{\Phi}{\Phi_0}}{\pi\frac{\Phi}{\Phi_0}}\right| \tag{1.7}$$
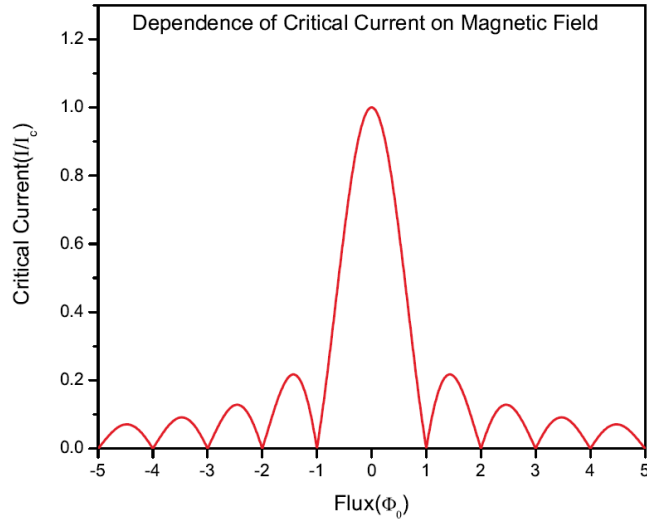
Figure 1.7: Critical current as a function of magnetic flux

The total critical current along the x-axis obtained from the current density forms a Fraunhofer pattern with respect to the flux threading through the junction Fig. 1.7.

8

The reaction to magnetic flux makes the Josephson junction a basic structure for most superconducting magnetic field detection devices [18].

1.5 SQUID

One of the most sensitive of these detection apparatuses utilize Superconducting Quantum Interference Devices (SQUIDs) [31], consisting of two parallel Josephson junctions connected by a superconducting loop, Fig. 1.8. Any small changes in external flux will lead to a voltage change in the SQUID which can be easily detected, bringing the sensitivity into the femtotesla range which is applicable to many different fields. During detection, the changing external magnetic flux Φ_a causes interference between the two junctions. This interference makes the critical current oscillate with the changing of the magnetic flux, Fig. 1.9. When biasing the SQUID with a current I_b, the critical current causes the voltage V across the SQUID to oscillate with respect to critical current modulation Fig. 1.10.

1.6 Flux-locked Loop

The voltage across the SQUID is strongly nonlinearly dependent on the magnetic flux. Fig. 1.11 shows the SQUID voltage with respect to applied magnetic flux. In order to convert this nonlinear SQUID transfer function into a linear one, Flux-locked Loops (FLL) are widely used [32–34]. The FLL generates a feedback signal to operate the SQUID at a fixed working point. The voltage across the SQUID will be amplified, integrated, and then
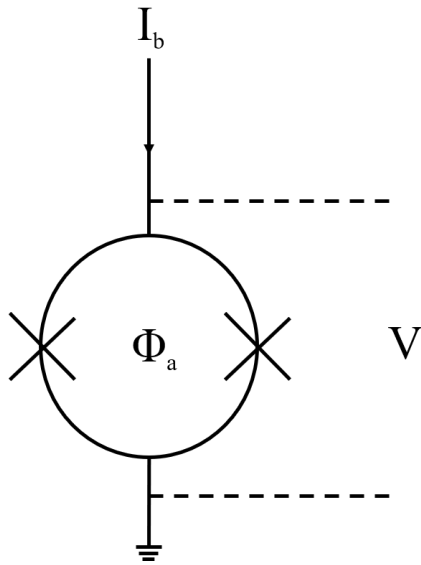
Figure 1.8: SQUID with bias current I_b, flux Φ_a, and voltage V.
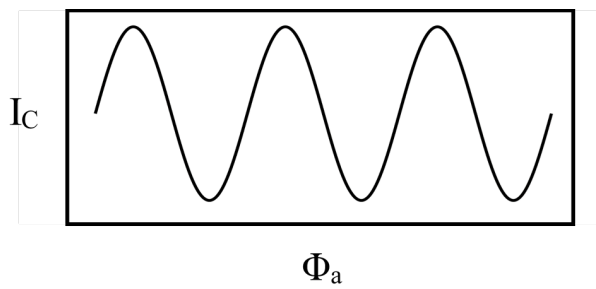
Figure 1.9: Critical current as a function of applied magnetic flux (Φ_a) for ideal SQUID.
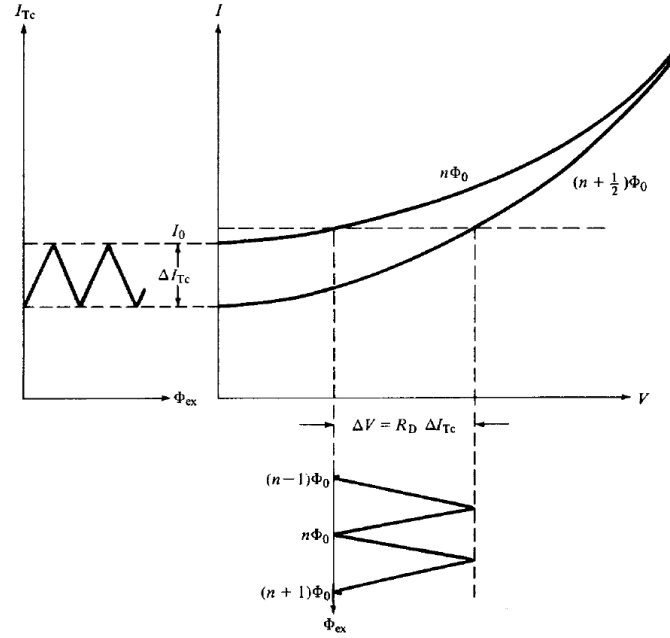
Figure 1.10: The current voltage characteristic for SQUID. The left graph shows the I_C changes with external flux and the bottom graph shows the corresponding voltage oscillation [18].
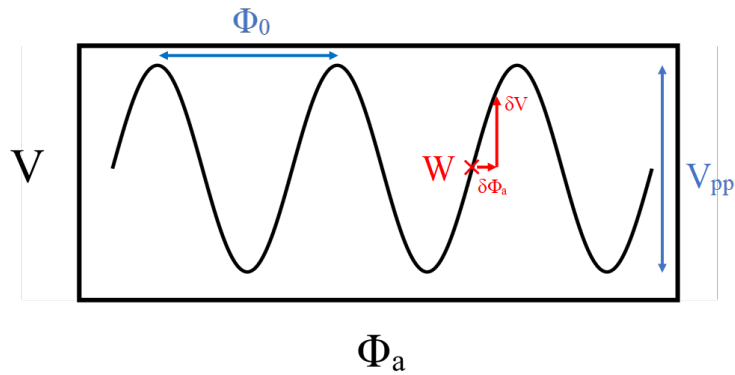
Figure 1.11: SQUID V–Φ_a characteristic with working point W [19]. Φ_0 is the flux quanta and V_{pp} is the SQUID transfer function amplitude. $\delta\Phi_a$ indicates the applied flux change and δV is the corresponding voltage change of the working point.

fed back into the coil which is inductively coupled to the SQUID, Fig. 1.12. The feedback

signal is linearly dependant on the applied flux at the working point and balances out the

external flux.
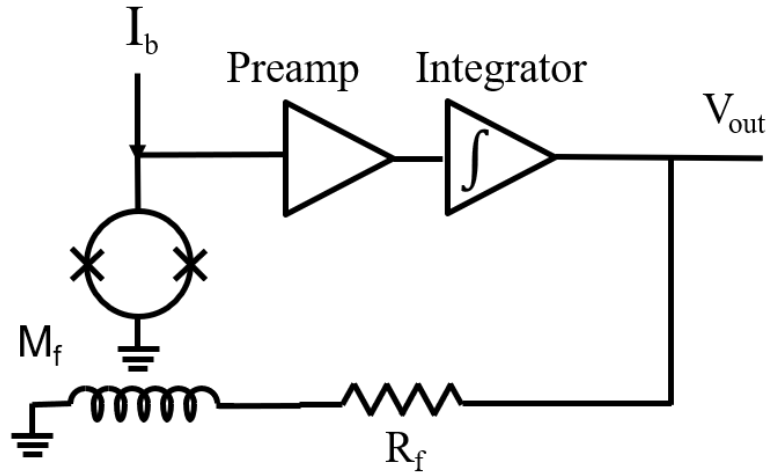
Figure 1.12: Basic FLL circuit.

1.6.1 Modulation

Due to the noise from amplifiers towards the low-transition-temperature (low-T_C)

SQUIDs [35,36], flux modulation is widely used in order to get a better transfer function out

of the system Fig. 1.13. Instead of one operating point, the feedback signal provides a square

wave modulation flux Φ_mod which operates the SQUID between W$^+$ and W$^-$ periodically.

Both working points W$^+$ and W$^-$ will be at the same voltage level without applied

flux. Any change in external flux will cause a modulating voltage signal from the SQUID

sensor. This AC voltage signal has same frequency as the modulation feedback signal, but
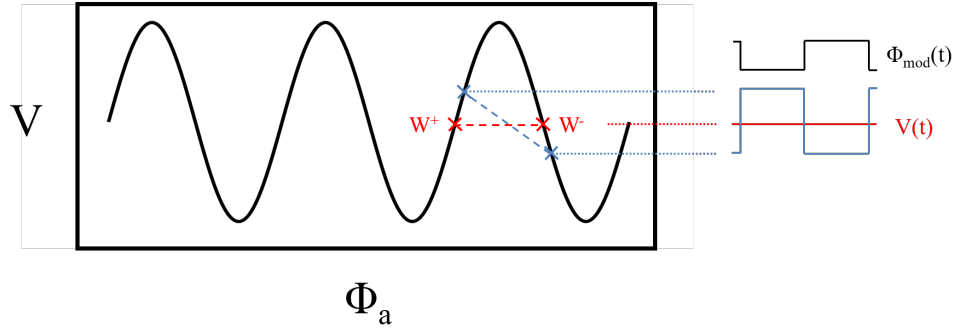
Figure 1.13: SQUID V–Φ_a characteristic with flux modulation. [19]. The flux modulation operates the SQUID between W$^+$ and W$^-$ which generates the same frequency voltage response while external flux is applied.

with a 180 degree difference if the external flux is in an opposing direction. The FLL with modulation typically uses a cooled step-up transformer to increase the voltage response and reduce the voltage noise coming from the transistor in the preamplifier. Then the system is directly connected to the preamplifier with a lock-in detector in order to detect the modulation frequency. The signal will then be integrated as in a basic FLL, combined with a modulation signal and then fed back into the SQUID.

1.6.2   Bias reversal
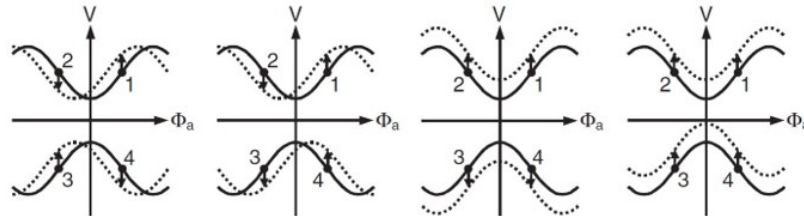
Figure 1.14: SQUID transfer function change under different circumstances. The black solid lines indicate the original V-Φ_a characteristics and the dotted the lines are the changes with applied external flux or other noise. The first from the left shows the effects from applied flux, second shows the changes from in-phase fluctuation, third is the out-phase fluctuation and the last one suggests the changes from pre-amplifier voltage noise [19].

Although, the fluctuation in critical current with normal resistance is weak in low-T_C SQUID, it is significant noise for high-transition-temperature (high-T_C) SQUIDs [37]. Fig. 1.14 shows the V-Φ_a changes under different circumstances [19]. In order to ignore the noise and only balance out the applied flux changes, current bias reversal is used to change the voltage response under situations other than external flux change into a different frequency [20, 38–42]. Fig. 1.15 is an example developed by Dossel *et al* [20]. The current bias and flux modulation operates the SQUID among four different points which generates a voltage response at a double modulation frequency. The SQUID voltage response will have same frequency as the the modulation frequency while under the effect of current bias and normal resistance fluctuation. A DC voltage will be shown across the SQUID if the noise is coming from pre-amplifier.
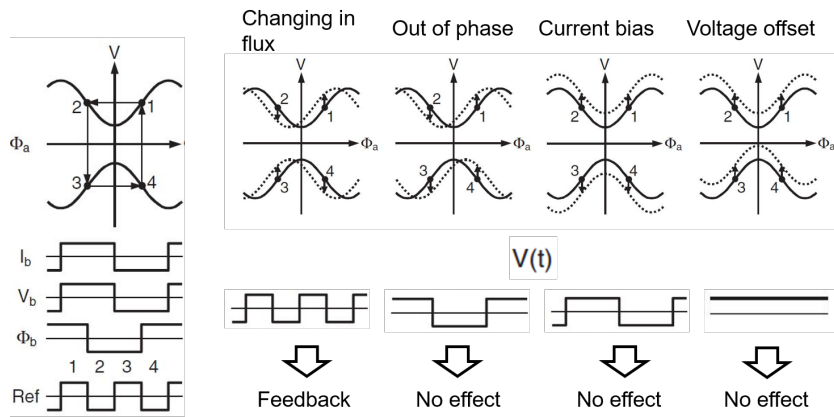
Figure 1.15: An example FLL circuit with bias reversal I_b and flux modulation Φ_b [19, 20]. The bias reversal is shifted 90 degrees from the flux modulation. When there is a change in applied flux, the voltage response modulates at twice the frequency of the flux modulation. For both in-phase and out-phase fluctuation from the bias current and normal resistance R, the voltage response is the same frequency as the flux modulation. The SQUID voltage response will be DC if the noise is coming from the pre-amplifier.

14

Chapter 2

Josephson Junction Magnetometer

2.1   Motivation

In many applications, a magnetometer with a high dynamic range and an impedance that matches most electronics has high demands. With the development of focused helium ion beam (FHB) technology, an approach using the HTS YBCO has been studied to provide a small size, weight, and power (SWAP) sensor with a high voltage response and the ability to operate unsheilded. Since typical Josephson Junctions have a size smaller than the Josephson penetration depth (λ_J) 4 µm, the supercurrent is distributed evenly throughout the junction, 2.1(a). The critical current forms a Fraunhofer pattern with respect to magnetic field as mentioned in chapter one.

The new approach uses a long junction which widens the Josephson Junction to a length that is much greater than twice λ_J, Fig. 2.1(b). As shown in 2.2, the self-field effect from the current changes the I_C-B curve into a more triangular shape with a higher
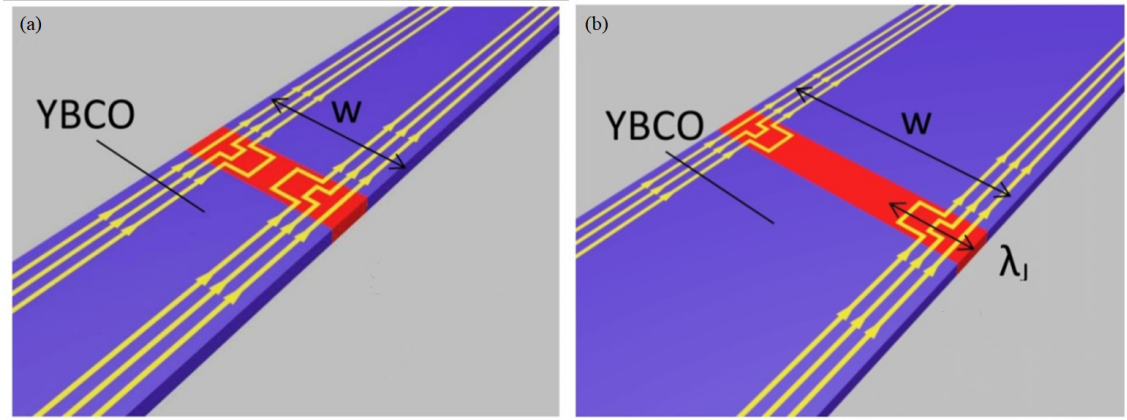
Figure 2.1: Schematic of a Josephson junction with (a) small width and (b) larger width. The red barrier on the YBCO indicates the junction and the yellow line shows the current flowing through the junctions.

linearity range [43–47]. The critical current change can be represented by the voltage across the junction with a factor of normal state resistance. Ideally, the slope of the curve could approach infinity by modifying the junction, which enhances the sensitivity (dV/dB) to detect small fields. In order to increase the voltage response, 1-dimensional long junction arrays have been designed. Connecting junctions in series also sums the voltage linearly with the number of junctions in series and leads to a higher signal to noise ratio (SNR) that improves the sensor's dynamic range [48,49]. In this chapter, the measurement of both long junctions and junction arrays will be demonstrated.

2.2   Measurement and Results

2.2.1   Long Junction

For a single long junction, thin film samples of YBCO were prepared and patterned into strips using photolithography and ion milling [50]. Small 1 to 30 wide bridges were
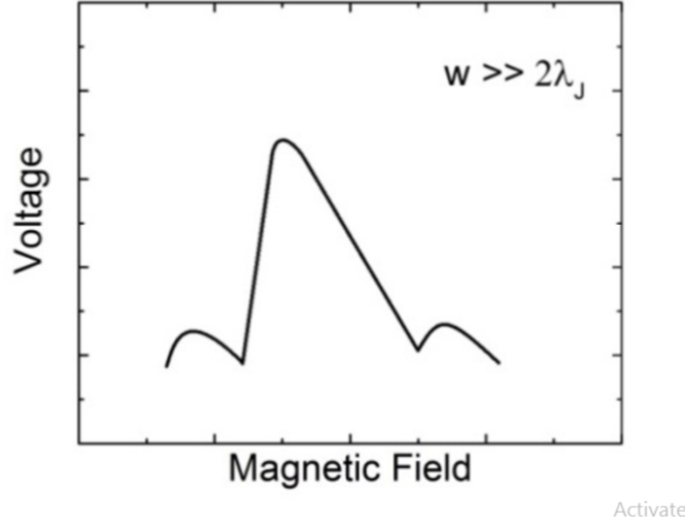
Figure 2.2: Critical current as a function of magnetic flux for long junction

irradiated across into single planar junctions using 30 keV focused helium ion beam with dose of $10^{16} \sim 10^{17}$ ion/cm^2.

Critical current as a function of applied magnetic field for junctions with different bridge widths were measured. For the narrow bridge width, the uniformity of the supercurrent in Josephson Junction leads to the ideal relationship between critical current response and external magnetic field, Fig. 2.3.

However, for wider long junctions, an asymmetric voltage behavior with a sharp edge and higher slope is observed, Fig. 2.4. Instead of the ideal Fraunhofer pattern, the I_C-V curve of 10 µm wide junction provides more linear regions on both sides. The dynamic range can cover up to 25 µT with a 200 µV output range. The sensitivity is roughly 4 V/T for this device.
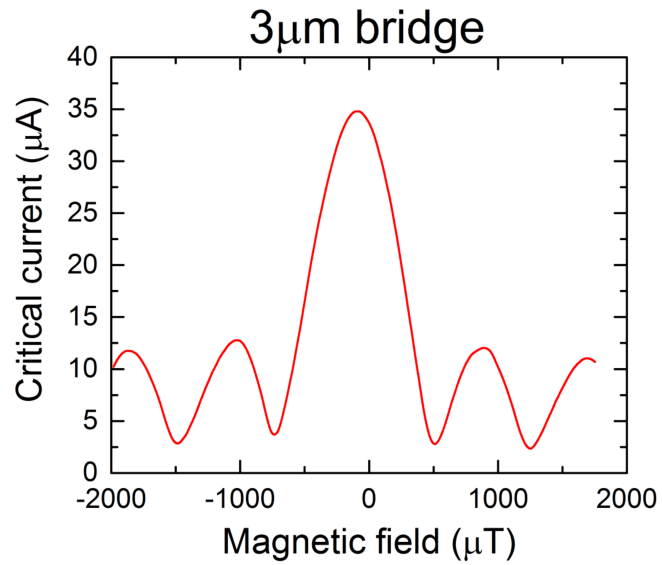
Figure 2.3: Critical Current as a function of applied magnetic field for YBCO thin film irradiated with 30 keV helium beam with 3 μm
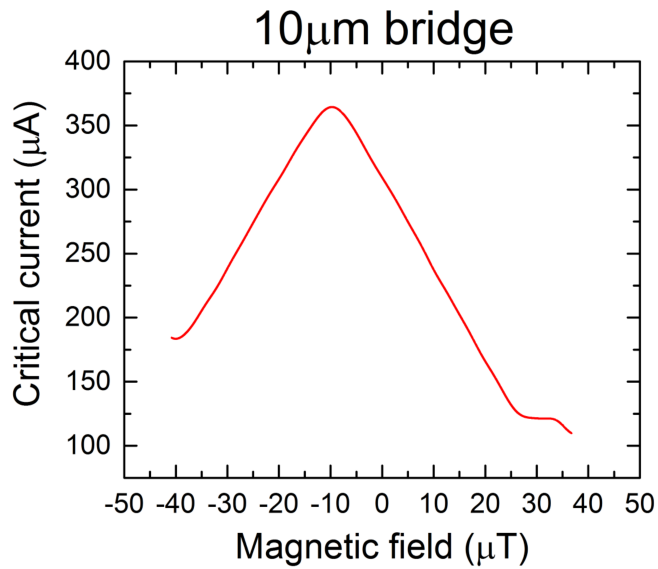
Figure 2.4: Critical Current as a function of applied magnetic field for YBCO thin film irradiated with 30 keV helium beam with 10 μm

2.2.2   junction arrayss

In order to increase the sensitivity as well as the voltage response, devices with 600 junctions connected in series were fabricated with 10 and 20 μm junction widths [50]. These devices exhibit a large, linear voltage response with applied magnetic field. The dynamic range is of the order of mT which is an improvement of three orders of magnitude over SQUID devices. This is sufficient for operation in Earths field (of 50μT).
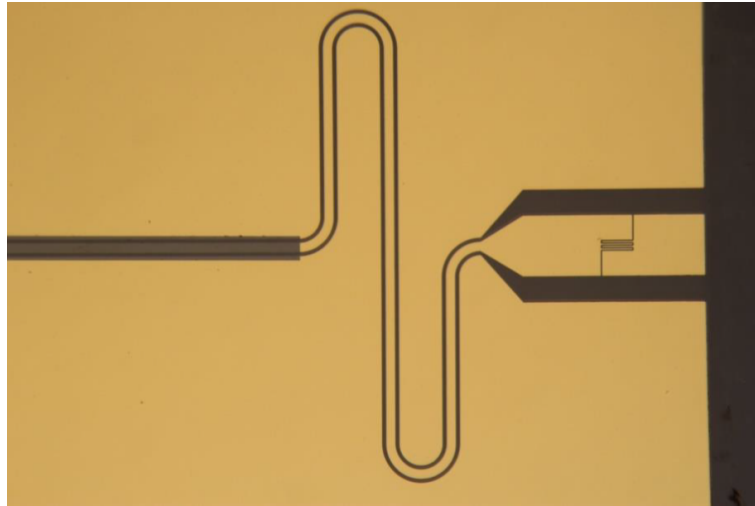
Figure 2.5: Optical photograph of YBCO strip and gold layer with the 600 junction arrays used in this study

Fig. 2.6 shows the V-B of 10 μm wide junction arrays operating around 61 K. To obtain an optimal characteristic, the junction arrays are biased just above the critical current. The linearity range provides about 20 μT with 12 mV dynamic range. The sensitivity can reach up to 500 V/T with a resistance of 90 Ω. The dynamic range could go up to 100 μT with a bijective relationship between Voltage and Magnetic field. This range is much larger than the Earth's field, which allows the long junction arrays to operate in an

unshielded environment. With additional electronics, this dynamic range can be increased

without reducing the sensitivities.
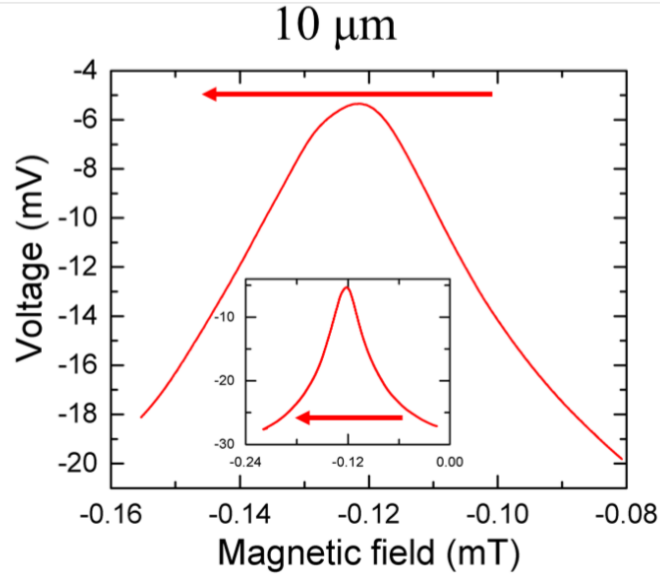
Figure 2.6: V-B curve of 10 μm bridge junction arrays at 61 K. A 10 μm bridge has a sensitivity around 500 V/T and a dynamic range around 100 μT. The insert graph shows the full dynamic range

Fig. 2.7 is the V-B curve of arrays with 20 μm-wide junctions. This device operates

around 73 K with a normal resistance of 35 Ω. The sensitivity is smaller compared to the

10 μm junction arrays, which is about 27 V/T. However, it provides a larger dynamic field

around 500 μT.

2.3   Discussion

This study provides a method to build highly sensitive devices with large dynamic

ranges that can operate unshielded in Earth's field for magnetic detection by using Joseph-
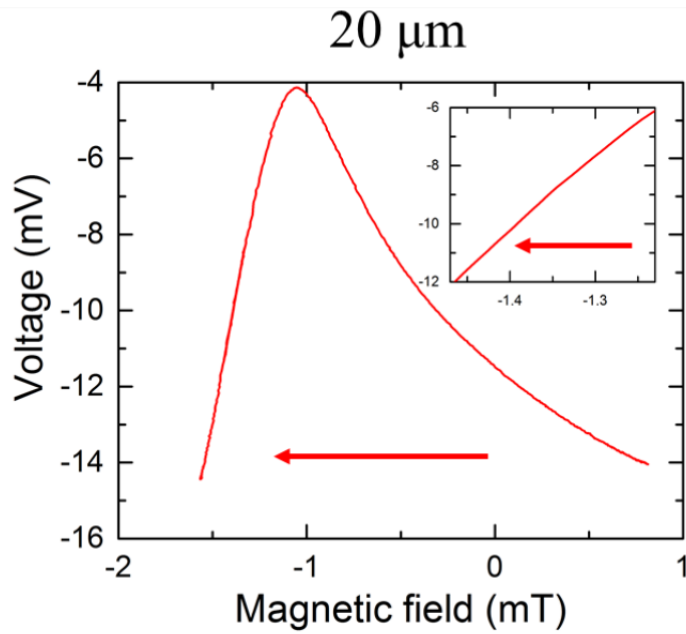
Figure 2.7: V-B curve of 20 μm bridge junction arrays at 73 K. 20 μm bridge has a sensitivity around 27 V/T and a dynamic range of more than 500 μT. The insert graph shows the linear regime.

son junction arrays. The magnetic field sensitivity is increased by putting junctions into series. Further study and analysis was done in Jay C LeFebvre's work [51]. The high voltage response of the junction arrays is enough to direct connect with electronic control systems. The impedance can be matched by changing the number of junctions in series to different kinds of electronics, and the dynamic range can be increased to a higher range also with additional electronics. A possible implementation to control long junction arrays will be discussed in chapter 5.

Chapter 3

SQUID Magnetometer

3.1 Motivation

One of the devices most sensitive to magnetic flux is the SQUID. As introduced in chapter one, the SQUID has two Josephson Junctions placed in parallel. The FHB provides the technology to build planer YBCO SQUIDs that can operate at higher temperatures. Developing a HTS SQUID would significately reduce the cost of building and maintaining the cryogenic system that runs LTS SQUIDs at around 4 K.

Due to the planer structure of the YBCO SQUID, current SQUID design uses two components to achieve both low noise and high field sensitivity. The first component is a nano-slit SQUID based on FHB technology. The smaller dimension of the SQUID can significantly reduce the flux noise [52, 53]. By bring the SQUID into the nano scale [53–57], the noise level can be reduced to below $1\ \mu\Phi_0/\mathrm{Hz}^{1/2}$. However, the field sensitivity is directly related the effective area of the SQUID. In order to remain or reach higher sensitivity, the effective area needs to be enlarged by concentrating flux into the SQUID, without

changing the SQUID dimension. Unlike LTS SQUID, where a multi-layer transformer can be implemented to concentrate the flux from a much larger area [58], a YBCO SQUID is limited by its planer structure. One of the widely used single layer approaches uses a direct injected pick-up loop [59, 60]. Fig. 3.1 shows a basic design of the direct coupled pick-up loop that shares an electrode with the planer SQUID. Just like the LTS SQUID, the pick-up coil forms a supercurrent from the magnetic flux. This superconducting current provides a flux that can be detected by the SQUID while flowing next to the SQUID hole. The effective area of the system is increased to $A_s + \alpha A_p L_s / L_p$ [61], where A_s and A_p are the area of the SQUID and pick-up loop and L_s and L_p are corresponding inductances of the SQUID and pick-up loop. The α is a constant factor based on supercurrent coupling. In most cases, the nano SQUID size is much smaller than the pick-up loop area and can be neglected. The effective ares is about $\alpha A_p L_s / L_p$. In D. Koelle's work [61], a 0.29 mm^2 effective area is created by direct coupling a 56 mm^2 pick-up loop. This approach retains the noise level of a nano SQUID and, at the same time, increases the sensitivity.

This direct injected nano SQUID design allows the YBCO SQUID sensor to operate at a relatively high temperature with high sensitivity and low noise. Higher temperature means that the sensor can be brought much closer to an object for a higher resolution magnetic field scanning compared to an LTS SQUID that operates at 4 K. The chapter will be focusing on validating the design of HTS SQUID, simulation and analysis for those direct inject nano SQUIDs, as well as the possible SQUID design for image systems.
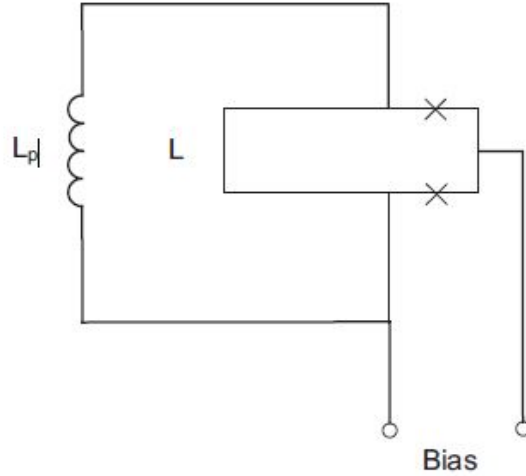
Figure 3.1: Schematic of SQUID with direct injected pick up loop [1].

3.2   SQUID Magnetometer

Fig. 3.2 shows a sample design of a direct injected YBCO SQUID. A more detailed description of its fabrication can be found in [62]. The SQUID design contains a 100 μm wide hexagonal pick-up loop with 10 μm wide bridge. It was structured by photolithography and argon ion milling of a 35 nm-thick reactive co-evaporated YBCO thin film. The SQUID loop and Josephson junctions were created using nanoscale focused ion beam materials modification of YBCO [26]. In a nanoslit-SQUID, a 10 nm × 50 μm slit is converted into an insulator by helium irradiation with a dose of 6×10^{17} ions/cm^2. The narrow slit serves as the SQUID loop. Two junctions are then written on either side of the loop with a lighter dose of 8×10^{16} ions/cm^2.

The inductance and current of the direct inject SQUID has been simulated using 3D-MLSI inductance simulation software [63,64]. In this simulation, the penetration depth
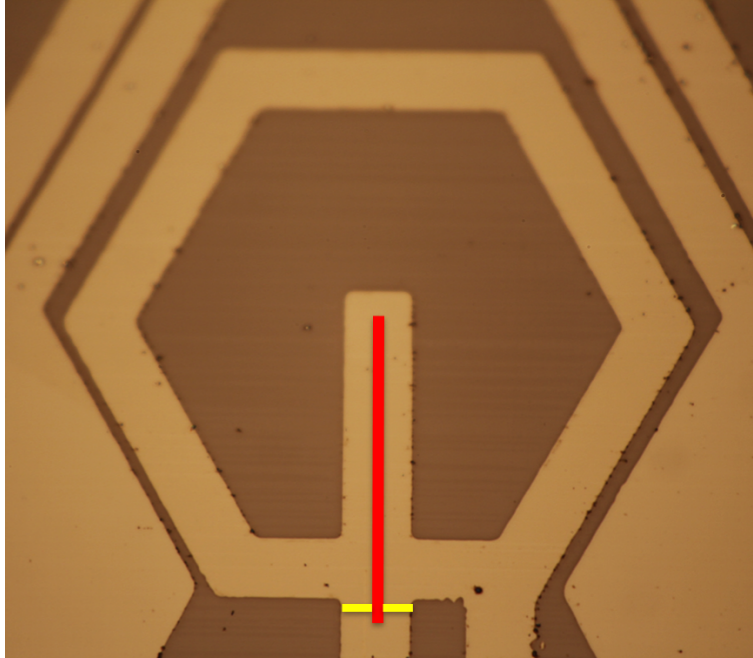
Figure 3.2: A direct injected nano SQUID design. The hexagon loop is the pick-up loop directly coupled to the SQUID. The red line indicates the area irradiated as the SQUID hole. The yellow lines are the two junctions written by the lighter dose FHB.

is set to 200 nm. Both resistances and SQUID junctions are not accounted for in the software's calculation. Fig. 3.3(a)-(b) shows the simulation for both the pick-up loop coil and the SQUID loop. The simulated pick-up coil has an inductance around 227 pH. The SQUID loop has much less inductance, about 58 pH, which gives a ratio of 1/4. With an α value around 0.8, the effective area is estimated to be about 1/5 of the hexagonal pick-up loop size, which matches our experimental data.

Fig. 3.4 shows the voltage response with respect to magnetic field for one of the YBCO hexagonal SQUIDs. The measurement is done around 9 K in the liquid helium with a μ-metal shield around the chip. Both current bias and temperature were adjusted in order to optimize the characteristics. The voltage response has a range of 90 μV with the static
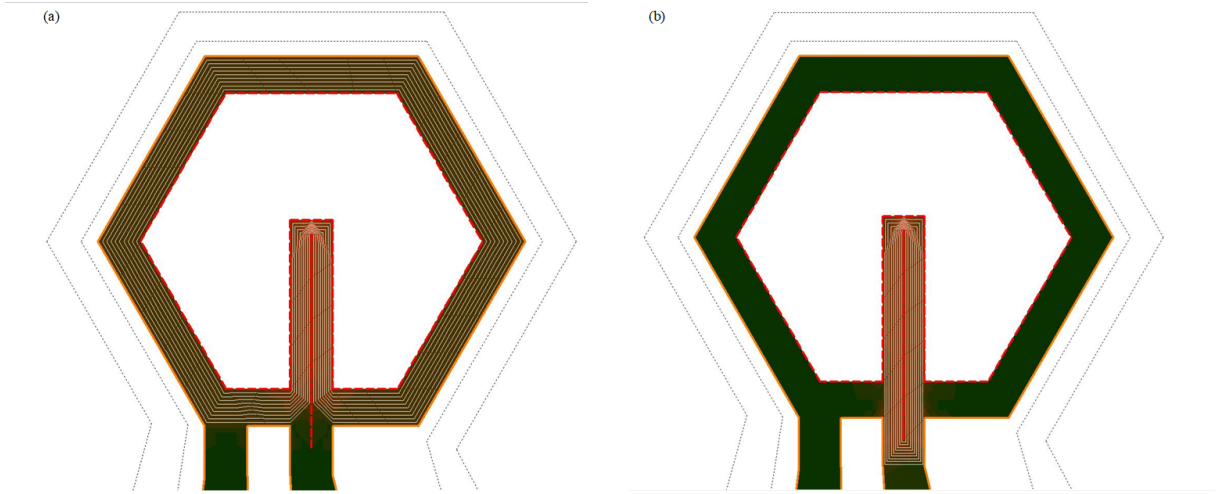
Figure 3.3: Inductance and current simulation for (a) the pickup loop and (b) the SQUID loop. White lines indicates the current follow. For the pickup loop, the inductance is about 227 pH and the SQUID loop in (b) has 58 pH.

current biased at around 12 µA. The linear region provides a sensitivity of up to 2.8 kV/T. Considering the period of 140 nT/Φ_0, the sensitivity towards the magnetic flux is about 390 µV/Φ_0. This specific sensor is designed for low temperature, however the same method can be used for SQUIDs to operate at higher temperatures by changing the dose of ion irradiation. One example is introduced below for the purpose of SQUID imaging.

3.3 SQUID Imaging

For further imaging applications, SQUIDs with rectangular pick-up coil has been designed. Those SQUIDs are placed at different angles, 45 degrees from each other. Fig. 3.5 shows the design of the SQUID. It has a 10 µm × 300 µm pick-up coil. The nano slit SQUID is about 20 µm long with 1 µm wide junctions on both sides. The operating temperature can range from around 40 K to 60 K. Fig. 3.6 indicates the V-B curve of one of the SQUID

27
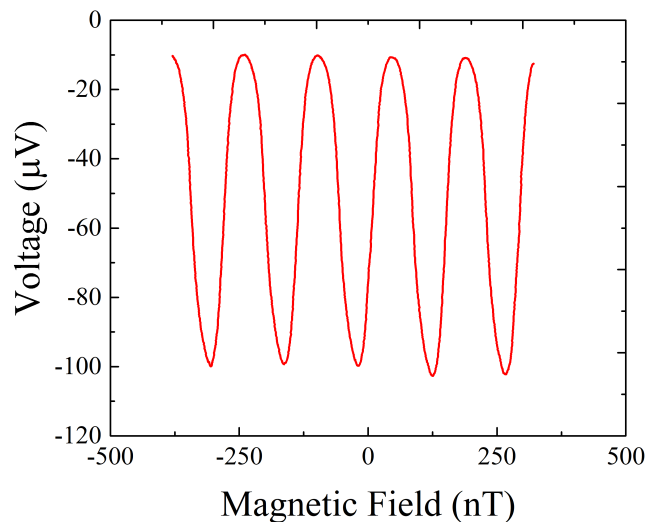
Figure 3.4: V-B characteristic of direct inject SQUID with hexagonal pick-up loop. The pick-up loop width is 300 μm.

operating at 62 K. The high operating temperature made it possible to measure in a small cryogenic system to provide a closer scan to the objects.

Imaging simulations have also been implemented to study the possible design of SQUIDs for higher resolution magnetic field detection. It is clear that the resolution of the SQUID image can be increased by implementing more SQUID sensors, smaller scanning steps, or using a smaller sensor size. With current YBCO SQUID technology, SQUIDs with different pick-up loops are simulated. The hexagonal SQUIDs with 100 μm width are designed into 2 by 2 SQUID arrays. The pick up loop area for each loop is about 750 μm^2 Fig. 3.7(b) is the simulated scan image results based on an image, Fig. 3.7(a), with a minimum feature size of 1 μm. The step of each scan is set to about 1 μm. The image is reconstructed by considering the surrounding SQUID data while scanning. Further image
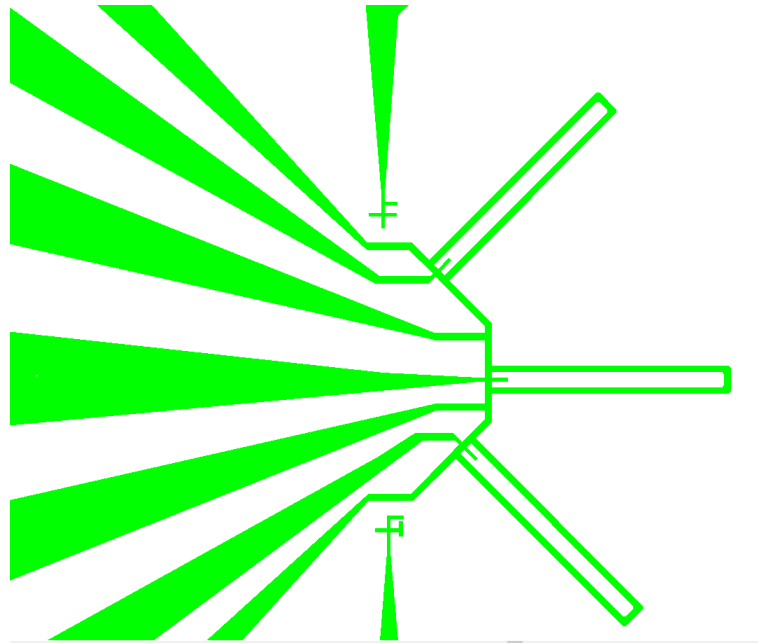
Figure 3.5: The rectangular SQUIDs in different directions 45 degrees apart. Just like the hexagonal design, the 10 μm × 300 μm large coil is the pick-up loop. The SQUID loop was irradiated down the bridge sticking out in the pick up loop. The junctions were written on the both sides of the back end of the SQUID loop.
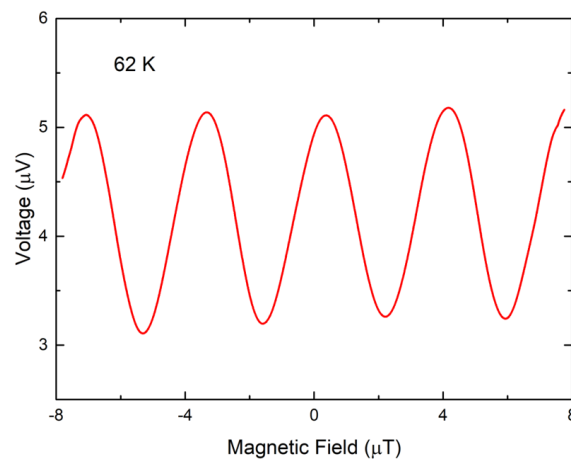
Figure 3.6: The V-B characteristic of one of the rectangular SQUIDs at 62 K. The nano SQUID loop length is 20 μm.

processing can been done with the storage of SQUID data in each position to increase the resolution. Fig. 3.7(c) provides a scan with an 87 μm wide square pick-up loop SQUID. The pick-up loop size is around 7569 μm^2 to compare with the hexagonal SQUIDs. It produced a similar resolution image under the same conditions as the hexagonal SQUIDs. Changing shape of the SQUID did not improve resolution on a large scale. Fig. 3.7(d) shows the result from a much smaller square pick-up loop SQUID with a size of 55 μ × 55 μm with all the other conditions remaining the same. It is obvious that reducing the SQUID size significantly increases the resolution of the image. Due to the SQUID sensitivity, the SQUID pick-up loop has a limited size for different electronics to provide the desired electronic properties. The simulation can be used to balance the SQUID properties with the image resolution for future SQUID magnetometer design.

Further simulations have been done to study the combination of images produced by changing the angles of long shape SQUIDs. The SQUIDs with rectangular pick-up loops have also been simulated with the same image. As mentioned above, the rectangular SQUID has a pick-up loop of about 300 μm × 10 μm. Rather than putting them into an array, they are designed into 4 different angles, 45 degrees from each other. In order to compare the result from the SQUID arrays scan, the same amount of SQUIDs are used in this simulation, one in each direction. Fig. 3.8(a-d) shows the simulated results from this design.

Even though rectangular SQUIDs have a much larger length when compared to the width of the square SQUIDs, the shorter side provides a more detailed resolution in each direction. Image processing can be implemented by taking all four scans into consideration. The 2 by 2 SQUIDs with square pick-up loops of size 55 μm × 55 μm have also been
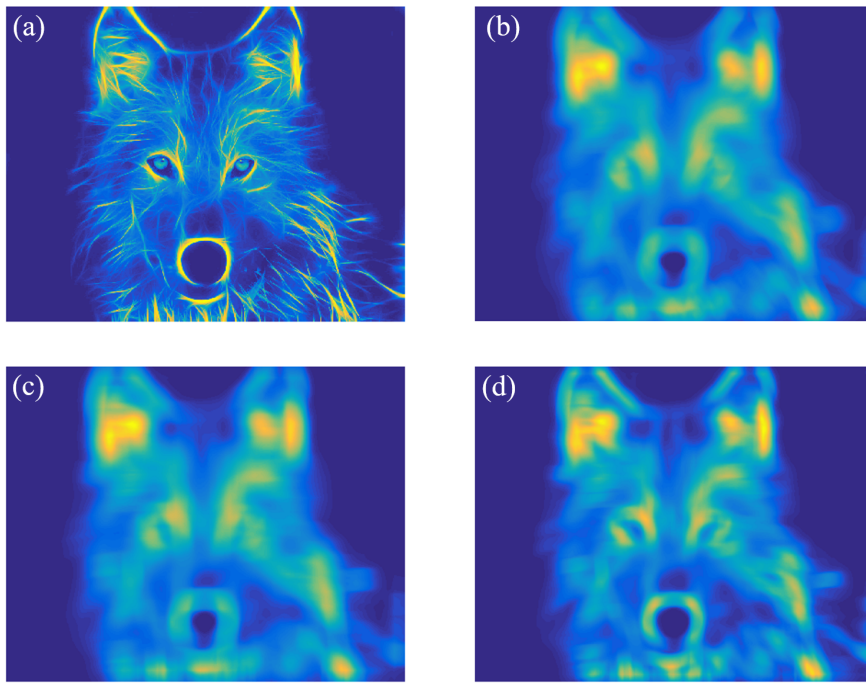
Figure 3.7: (a) Original image with a minimum feature about 1 µm, (b) simulated image scanned with 2×2 hexagonal SQUIDs, (c) simulated image scanned with 2×2 square SQUIDs, and (d) simulated image scanned with 2×2 square SQUIDs with pick-up loop size 2.5 times smaller than the SQUID in (b) and (c). Each pixel in original image is considered to have a size of 1 µm $\times$ 1 µm, which gives a total size of 1.2 mm $\times$ 1.6 mm.
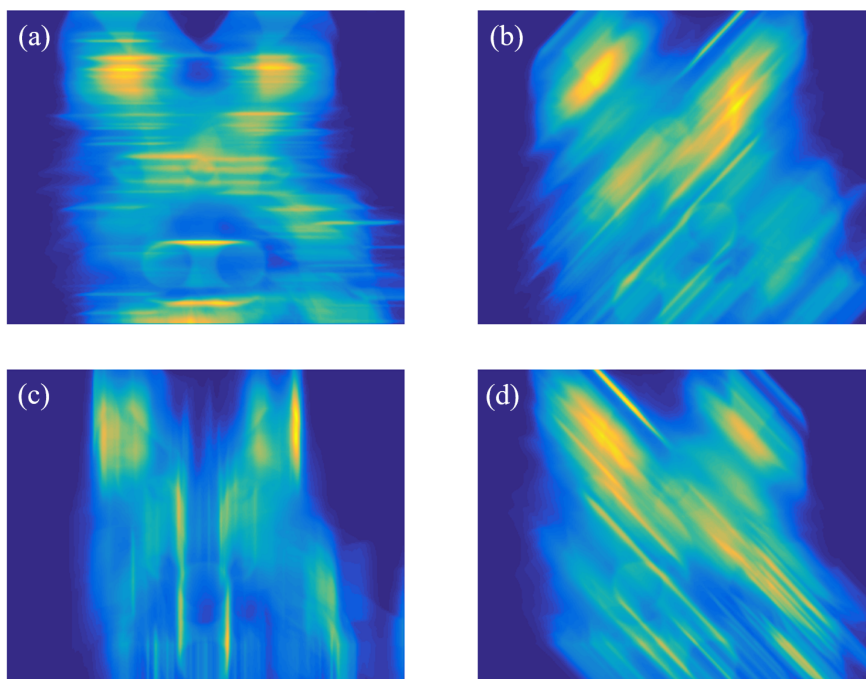
Figure 3.8: Image simulation of SQUID scan for 10 μm × 300 μm rectangular SQUID with (a) 0 degree rotation, (b) 45 degree rotation, (c) 90 degree rotation, and (d) 135 degree rotation.

simulated to compare to the reconstructed rectangle design. Both pick-up loops have about 3000 μm² in area. The SQUID pick-up loop size is 3 orders of magnitude larger than the minimum feature size of the target. It is obvious that the reconstructed rectangular SQUIDs scan contains more details than that of the same size square SQUID.
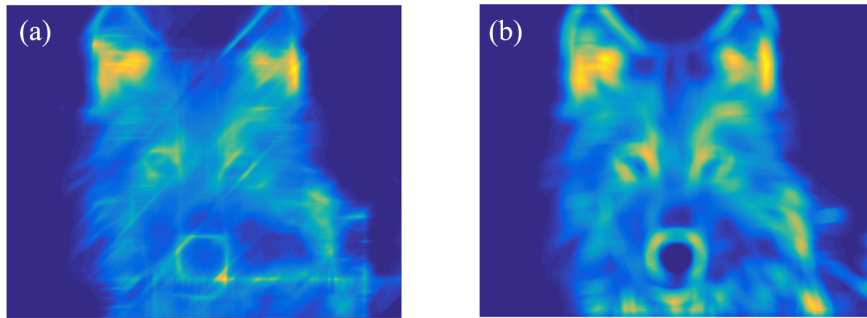
Figure 3.9: (a) Reconstructed image from four ractanguler SQUIDs scan data. (b) The image simulation of 2 by 2 square SQUIDs. The square SQUID has the pick-up loop size about 55 μm × 55 μm to match the size of the pick-up loop of the rectangular SQUID.

3.4   Discussion

In this chapter, nano SQUIDs with various shapes of direct injected pick-up coils were tested. The electronic properties were studied for further SQUID design and electronics matching. The ability to control the temperature, resistance, and inductance properties of the SQUID provides the possibility of wide ranges of application. For SQUIDs with voltage responses of up to 100 μV, or even higher, operating at a relatively low temperatures, the voltage noise from the pre-amplifier can possibly be ignored. Direct readout electronics can be used without a cooled step-up coil. Possible solutions for SQUID magnetometer array design for magnetic field imaging has be simulated. The study indicates that SQUIDs with

rectangular pick-up loops in different directions may produce better resolution compared to 2 dimensional square or hexagonal SQUID arrays with the same size and the same total amount of SQUIDs. This could be a solution for high resolution SQUID scanning. Moreover, with the development of HTS SQUIDs, the sensors can be placed much closer to the patient or the object by distance. A combination of different types of SQUID magnetometers will very likely provide an even higher resolution image.

It is clear that a multi-SQUID electronic control system is necessary for parallel processing of real time SQUID data, real time calculation, and further signal processing. Large SQUID systems already exist, such as magenetoencephalography (MEG), which uses more than 300 LTS SQUIDs at liquid helium temperature. These systems are still using the traditional analog FLL in order to control the SQUIDs. These 300 FLL systems will need to connect to a computer one by one in order to process the data. One traditional FLL can not operate both LTS and HTS SQUIDs. The components need to be modified to operate sensors with different electronic properties for different applications. A scalable system with strong processing capability and adjustable parameters will be ideal for SQUID imaging and analysis. In chapter 5, a new approach will be discussed in detail.

Chapter 4

SQUID Arrays

4.1   Motivation

As with the Josephson Junction arrays, the voltage across the SQUIDs will also sum linearly in series. The critical current can be increased simultaneously by putting the SQUIDs in parallel. By designing 2D SQUID arrays, the impedance can be easily controlled by modifying the array size in both dimensions. This can be a possible approach to applications [7, 65–67] requiring high voltage responses with large dynamic ranges and matched impedance [9, 68–71]. In this chapter, both simulation and data analysis are implemented to gain a deeper understanding of the electronic properties of the SQUID arrays.

4.2 Simulation

In this study, the simulation and data analysis are based on two types of SQUID arrays designed, fabricated, and measured in the work of Ehtan Cho [21, 72]. As shown in Fig. 4.1, both close-packed and segmented SQUID arrays have 1 to 9 rows of 1000 SQUIDs in parallel. Both designs have a 2 μm distance between the SQUIDs and the boundary with 3×3 μm^2 SQUID loops. Unlike the close-packed chip in which the SQUIDs are directly connected, the segmented chip separates each column of the SQUIDs and connects them using a 4 μm wide bridge. Those arrays are fabricated on 150 nm YBCO thin films. The chips used 200 keV neon ions with a dose of 2×10^{13} ions/cm^2 to irradiate the YBCO to create the Josephson Junctions.
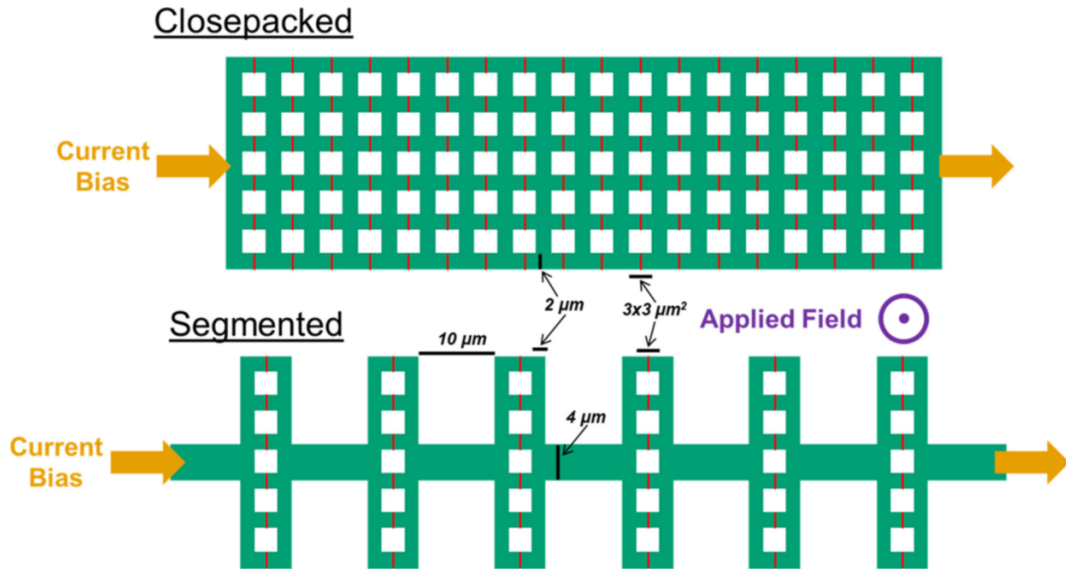
Figure 4.1: Close-packed and Segmented SQUID array designs. There are 1000 SQUIDs in each row. The row number of the SQUID arrays range from 1 to 9. The SQUIDs are 2 μm away from each other and the SQUID loop size is 3×3 μm [21].

During the measurement, a bias current was applied through the SQUID arrays. Voltage response was measured with applied magnetic field under temperatures ranging from 45 K to 77 K. The voltage response range was adjusted to the largest set by changing the bias current and temperature to maximize the V-B characteristics. Fig. 4.2(a) shows the V-B curve of the 8 × 1000 close-packed SQUID arrays operating around 49 K. The voltage modulation increases to around 2.5 mV with a sensitivity up to 90 V/T. As shown in Fig. 4.2(b) the segmented design of the same size has a similar result. With an operating temperature around 45 K, the array provides about 2.8 mV voltage response with a maximum sensitivity around 118 V/T.
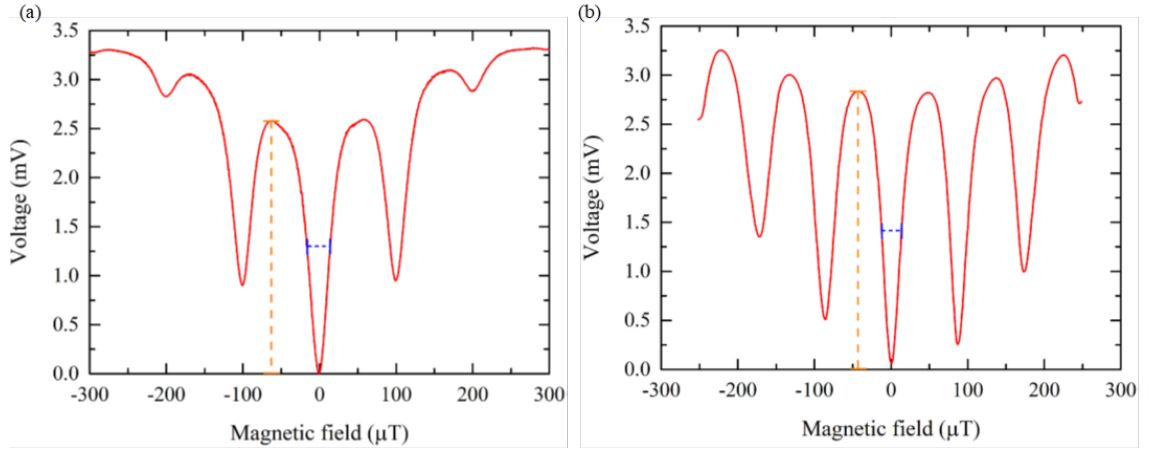
Figure 4.2: Voltage with respect to magnetic field of (a) close-packed SQUID arrays and (b) segmented SQUID arrays [21].

To have a deeper understand of the electronic properties, current simulations were done on both designs using 3D-MLSI [21]. The penetration depth in the simulations was set to 200 nm with a 1 μA current flowing through the array. Both resistances and SQUID junctions are not accounted for in the software's calculation. Fig. 4.3(a)-(c) shows the

current simulation result with an external flux range from 0 to 1/2 flux quanta in the real size.

When there is no external magnetic flux for close-pack SQUID arrays, the current is evenly distributed across the SQUID. But in the segmented SQUID arrays, the current is distributed more closely to the center line. After applying magnetic field, the current in both geometries are distributed evenly along the SQUID with similar self circling current. This phenomenon likely arises because the space between the SQUIDs are much larger than the set penetration depth. Devices are then simulated at 20 times smaller in both dimensions compared to the original device. The size of the SQUID loops now become 150 nm *times* 150 nm with an 100 nm electrode in between. The width of the electrode is much smaller than of the set penetration depth (200 nm). As shown in Fig. 4.4 (a-c), the same conditions were applied in this simulation, providing applied flux from 0 to 1/2 Φ_0. In this simulation, the close-packed geometry has the same uniformly distributed current that is not affected by magnetic field, but the segmented arrays have a high current density concentrated in the middle electrode.

Additional current simulations have been implemented with the same conditions as the previous simulations for close-packed designs but with additional Johnson Junctions taken into considerations. The junctions were simulated by modifying the height of the YBCO films and the penetration depth of the narrow regions on the SQUID loop. Under these conditions, the current will be distributed evenly on the simulated junctions. Fig. 4.5 is the results of 2×5 and 5×5 close-packed SQUID arrays. A current of 1 μA flows from the left side to the right and the current density flows into the junction areas within the range
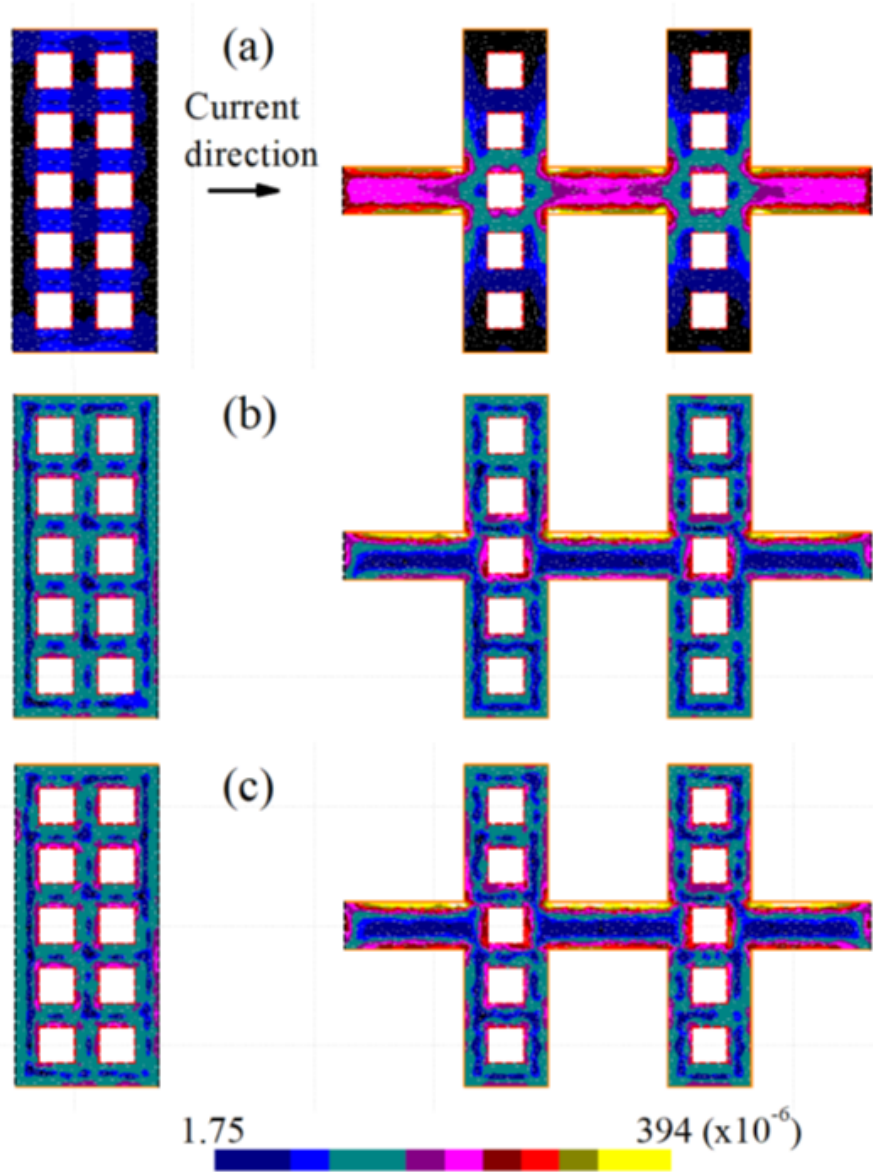
Figure 4.3: Current simulation for 5 SQUID rows with (a) no external magnetic flux, (b) 1/4 flux quanta (c) 1/2 flux quanta. A Current of 1 μA flows from left to right in both design [21].
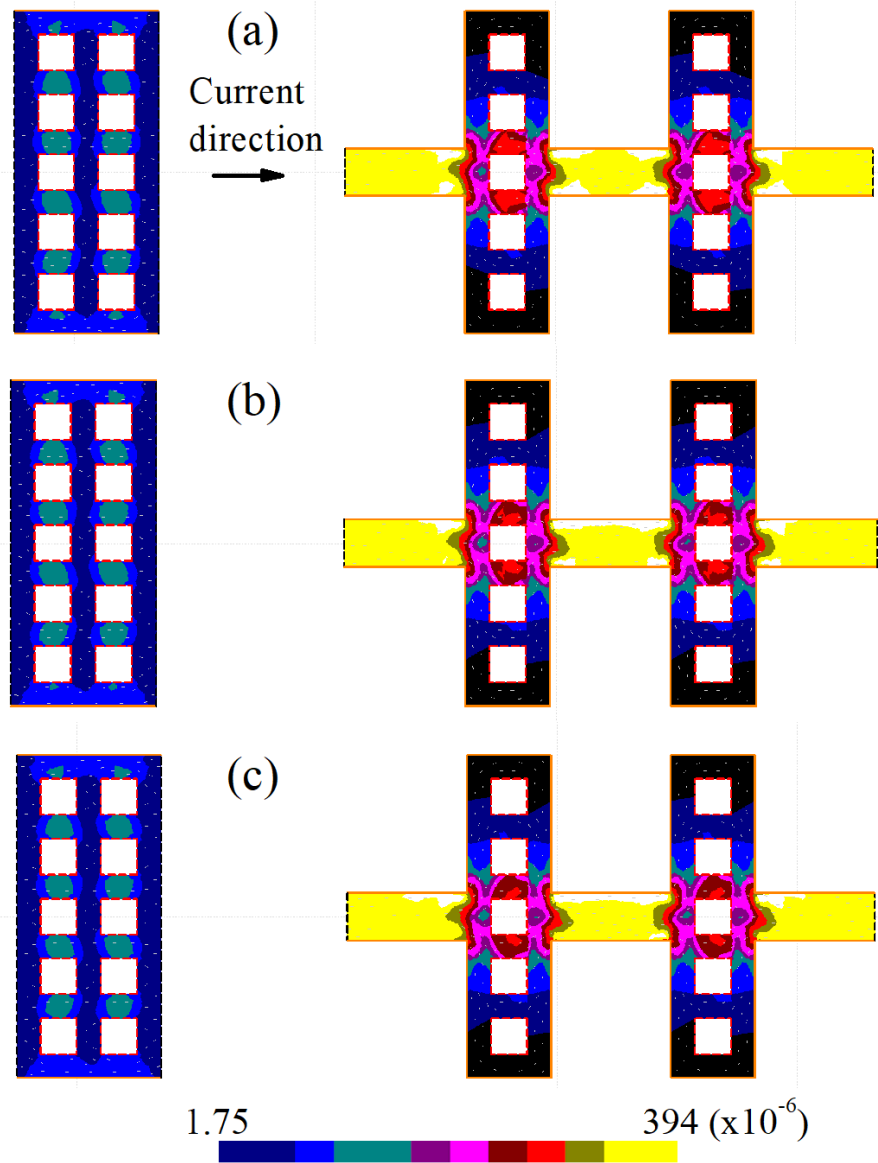
Figure 4.4: Current simulation for smaller size 5 SQUID rows with (a) no external magnetic flux, (b) 1/4 flux quanta (c) 1/2 flux quanta. Current flows from left to right in both design. The total size is reduced 20 times. Each SQUID hole is reduced to 150 nm in width and the electrode is about 100 nm, about half of the penetration depth [21].

of 200 nm penetration depth on each side. Especially in Fig. 4.5(a), the light green region

can be clearly seen that relatively equal amount of current density is distributed through

the junction area. If the array is cut in order to look at the cross section of the junctions,

the current distribution is shown in Fig. 4.6. In ideal cases, the current distribution should

be roughly the same on each junction. Due to the size of triangular mesh used in the

simulation, the current density is not smoothly distributed over the simulated junction.

Various simulations have been done to prove that the results are randomly distributed due

to the different meshes used in the different columns. In the real SQUID array, the current

density in one column of junctions is highly likely to be randomly distributed, just like the

simulated data. But the general distribution of 1000 SQUIDs in series should not be as

random.
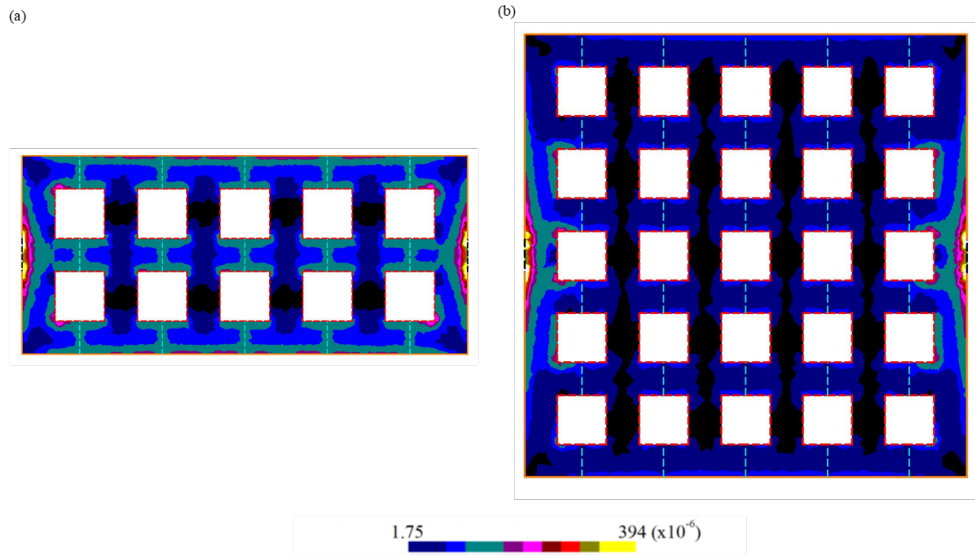
Figure 4.5: Current simulation for both 2 and 5 rows of SQUID arrays with junctions. The
light blue dash line indicates the Josephson junctions.
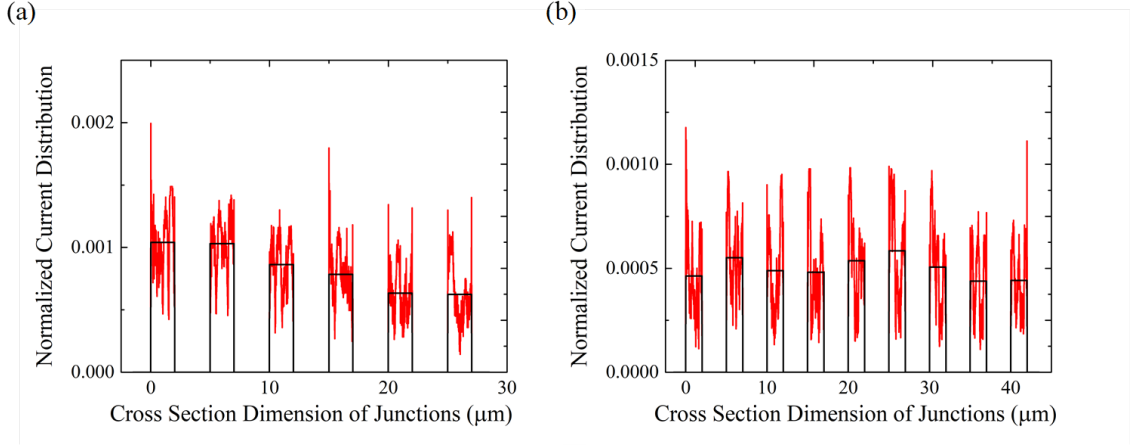
Figure 4.6: The normalized current distribution at the cross section of junctions for (a) 5 rows of SQUID arrays and (b) 8 rows of SQUID arrays. The red line is the current distribution from the meshes in simulation and the black line is the average of each current block.

In order to obtain the general current distribution, the interference effect in the junctions arrays is studied. Just like the Young's double slit experiment, for a row of SQUIDs, the voltage modulation in changing magnetic field is the interference pattern on the screen. The real current distribution with respect to effective area can be estimated by fitting a Fourier transform of current distribution with respect to effective area into the V-B curves of the close-packed SQUID arrays. The data can be matched to different current distributions with an extremely low error rate. Fig. 4.7 shows one set of the current results of the V-B curves regression for 1 to 6 SQUID array rows. Multiple sets of solutions for current distribution exist in the fitting because of the loss of the imaginary part of the signal and the wide range of the data. Considering that the V-B is formed from a 1000 arrays in series, we would assume that the current vs. effective area is uniformly distributed.
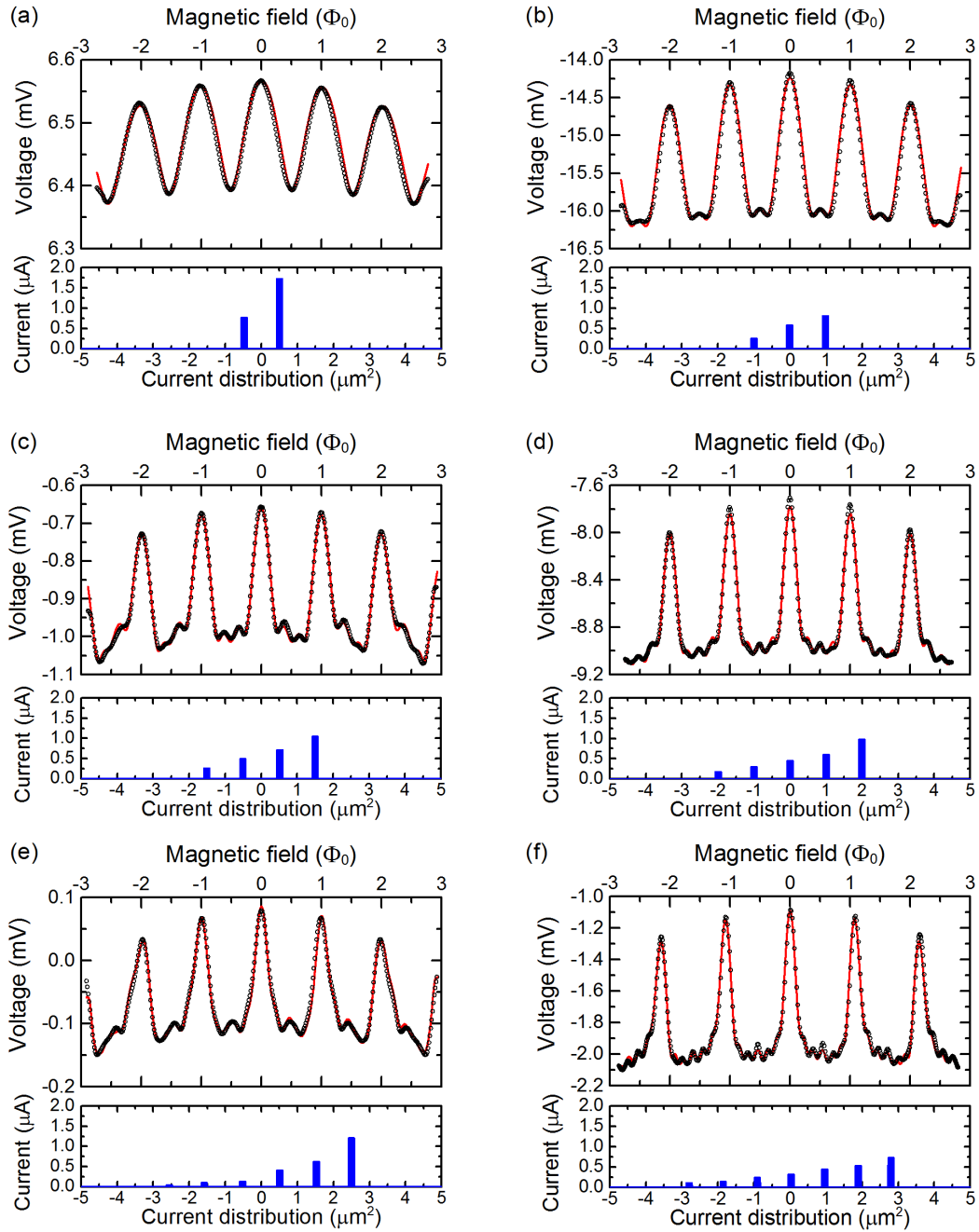
Figure 4.7: (a)-(f) show the V-B curve and the fitting curve with corresponding current distribution for 1 to 6 rows of SQUID arrays. The black dots are the original V-B characteristics of the SQUID arrays. The black line is the fitting data as well was the Fourier transform of the current distribution. The blue bars are the current distribution with respect to effective area

43

However, based on the shape of the V-B curve and the fitting result, the current distribution is highly unlikely to be evenly distributed at each junction area.

4.3   Discussion

In this chapter, electronic properties of SQUID arrays have been studied based on previous measurements. Current distributions are simulated for both geometries in two different sizes to provide further knowledge in SQUID array design. For close-packed SQUID arrays, the dimensions of the SQUID loop and electrodes do not have much effect towards the current distribution. The characteristics should remain the same. However, when reducing the size of the segmented SQUID to much less than penetration depth, the current is concentrated on the center of the SQUIDs and bridges. This may bring significant changes to the characteristic of segmented SQUID arrays. This suggests that the size of spacing between SQUID arrays have a minimum size based on the penetration depth in order to retain their their functionality. The interference effect in parallel junction arrays has be studied by fitting the V-B curve to Fourier transformed current distributions in effective areas. Multiple possible solutions exist based on the data we obtained. With the accumulation of a 1000 SQUIDs in each row, the current density is still not evenly distributed. The factor that dominates the current distribution is still an open question that needs to be studied.

4.4 Acknowledgement

Chapter 5

Electronic Feedback System

5.1 Motivation

Magnetometers based on Superconducting Quantum Interference Devices (SQUIDs) are amongst the most sensitive detectors of magnetic field. They have been widely used in geological, biomedical, and electromagnetic analysis [73, 74]. Many applications require a large number of sensors, high dynamic range, high-slew rate, and communication over large distances for parallel processing. However, most SQUID control systems lack some of these features because they are based on analog flux-locked-loop (FLL) feedback electronics [75, 76]. While analog FLL systems demonstrate the lowest noise, there are drawbacks that complicate operating and processing data from large numbers of sensors. Unlike an analog FLL, a digital FLL does not require the use of multi-position switches in order to change the feedback resistors or time constants. This is a highly desirable feature in large scale multi-sensor systems. Moreover, for sensors with different electrical properties, dis-

tinct analog circuits have to be designed and customized to each type of sensor for optimal performance. Digital based feedback electronics could alleviate some of these drawbacks.

Previously, Oyama *et al.* developed a digital FLL system using a double counter method in order to measure an unsheilded SQUID [77]. It exhibited a large dynamic range up to 141 dB at 1 Hz, however, the digital feedback loop experienced a substantial delay of 8.4 µs that limited the bandwidth. Then, Ludwig *et al.* developed an improved digital SQUID feedback system using complex programmable logic devices (CPLD). [19, 78] This approach reduced the delay time to 200 ns albeit still much larger than analog systems which typically have values of 15 ns [19].

The rapid advancement in the performance of high-frequency digital components driven by the mobile communications industry motivates the further development of digital flux locked loop (DFLL) technology. In order to develop a new generation of DFLL for both low and high-transition-temperature (high-T_C) SQUIDs, we employed a digital electronic feedback system using Field Programmable Gate Arrays (FPGAs) [79, 80]. FPGAs are re-programmable integrated circuits suitable for high performance computing, data storage, and high-speed communication. FPGAs have the potential to solve many of the problems present in various applications. The mixed response signal of flux modulation and current bias can be demodulated and recovered through the digital system using digital signal processing (DSP). An additional digital filter can be added, and further DSP can be used for SQUID data analysis, including multi-SQUID processing, digital gradiometer subtraction, and SQUID imaging. In this work, we implemented an FLL algorithm using an FPGA to operate a high-T_C direct inject SQUID [62].

5.2   Design

Fig. 5.1 shows a general schematic for the basic set-up of our DFLL. The Xilinx Spartan 6 FPGA generates a modulation signal using a 16 bit digital-to-analog converter (DAC) that is inductively coupled into the SQUID. The SQUID voltage is amplified using a low noise preamplifier and is filtered to bandpass the frequency. That output is then fed into an analog-to-digital converter (ADC) for demodulation redof current bias frequency and digitization into a 16 bit digital signal [81]. The FPGA demodulates the digital signal and functions as a smart FLL which locks the SQUID at a programmed voltage range. Using a 16 bit DAC, the FPGA subsequently generates a feedback signal which is then sent to the feedback coil of the SQUID in order to null the external magnetic field changes.
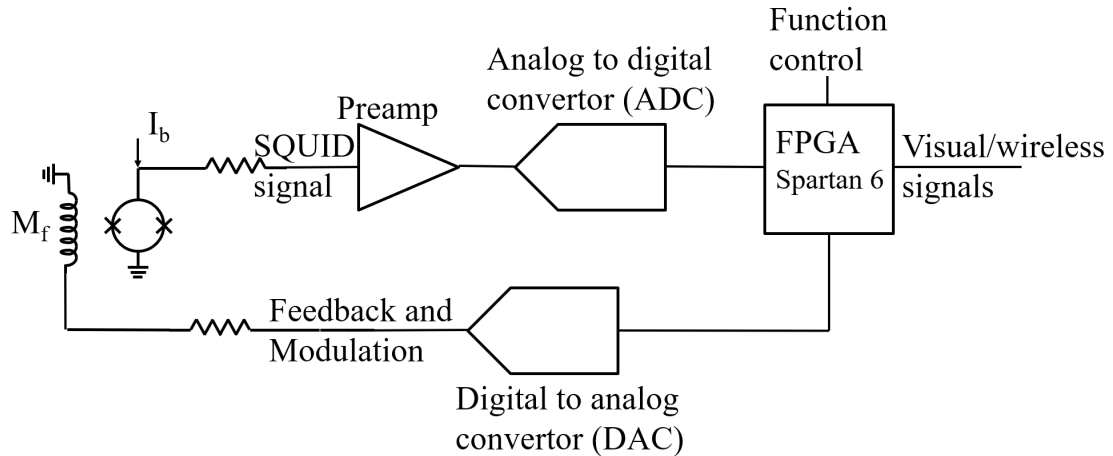
Figure 5.1: Schematic for FPGA based digital flux locked loop.

The ADC, with four input pairs per chip, has a high sample rate, up to 100 MSPS, for a wider bandwidth. The capture delay is about 3 ns. The FPGA delay for a specific

algorithm is about 21.35 ns plus the user-set integration period. The DAC we used has four parallel outputs with a settle time of about 20 ns. Operating the system at around 10 MHz without considering the delay in the wires connecting back to the SQUID coil, the slew rate can be as fast as 3.46 MΦ_0/s. The actual slew rate will be slightly smaller due to transmission line propagation delay (about 5 ns) [19]. For a 2 m transmission line, we estimate a maximum slew rate of 3.0 MΦ_0/s. This slew rate can be further increase with an additional digital counter.

5.3 Theories

From chapter one, there are multiple current bias methods that could be used to implement this design. Other than that, two other approaches are shown below with the advantages of the digital system.

The first one is an implementation of AM demodulation. By current bias reversal at a much higher frequency, the SQUID works as a mixer. Fig. 5.2 shows the voltage signal produced by mixing both sinusoidal current bias and flux modulation by the SQUID. The signal can be sampled at the same frequency of current bias in ADC to reconstruct the voltage modulation with respect to magnetic field. The reconstructed voltage can be demodulated again to reconstruct the external magnetic flux change on the working points. Square-wave modulation in both bias reversal and flux modulation will work the same as sine waves. A benefit from this approach is that other frequency noise can be filtered out before demodulation. The drawback of this approach is that, based on the

current bias analysis, out of phase change in current bias fluctuation may still exist in this implementation producing a relatively high noise in (high-T_C) SQUIDs.
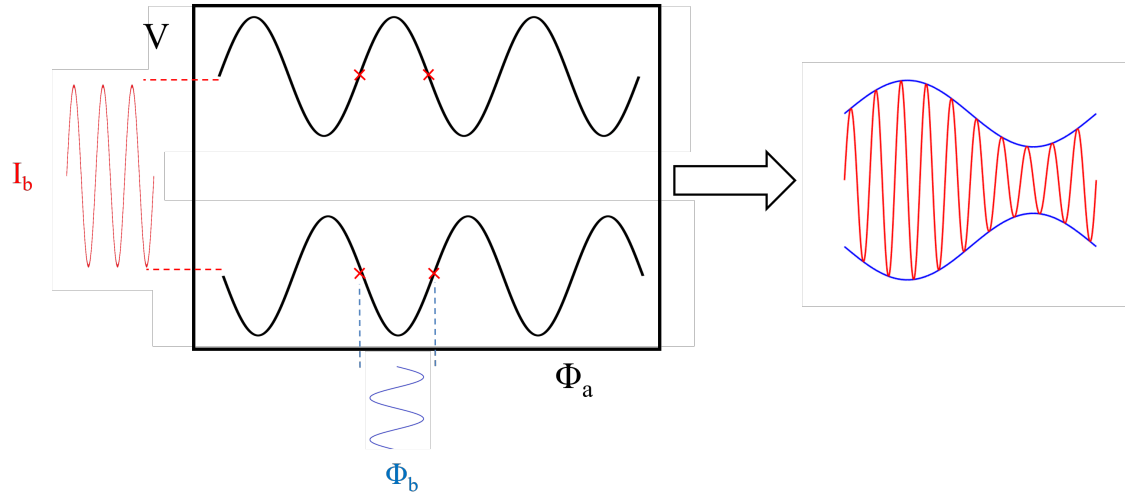
Figure 5.2: The left graph is the V-B characteristic of SQUID at two different bias stage. By appling current bias I_b with flux modulation Φ_b, the SQUID output is a mixed amplitude modulation signal.

The other approach is a voltage approach based on the traditional FLL current bias and modulation. With the capability of storing data in FPGA, the SQUID data can be analyzed during the scan providing linearity, sensitivity, voltage level, etc. on each point of the V-B curve. This feature function can be applied to other methods as well to improve the linearization of the transfer function. Based on this, by providing a voltage difference between working points on each biased current in the FPGA from a previous scan, precision locking on flexible working points can be achieved. Fig. 5.3 shows the voltage response and the calculation done in the FPGA to cancel out different noise. The current bias is modulating at twice flux modulation frequency or even higher. The SQUID output signal is sampling at a much higher frequency than the bias reversal. The $V_\Delta(t)$ is the voltage

difference between the working points at the same flux bias but at different current bias levels. This value will be subtracted by the original voltage difference between the same points $V_{\Delta i}(t)$, which is calculated from the scanning period. If the result has the same frequency as the modulation, the voltage difference will be integrated and then fed back to the SQUID to balance out the external flux. Other noise such as current fluctuation or voltage bias would not produce a feedback change. This method can bring the working points at different flux bias stages to a different voltage level. It is suitable for sensors with transfer functions that have linear regions and high sensitive areas that are asymmetrically distributed.
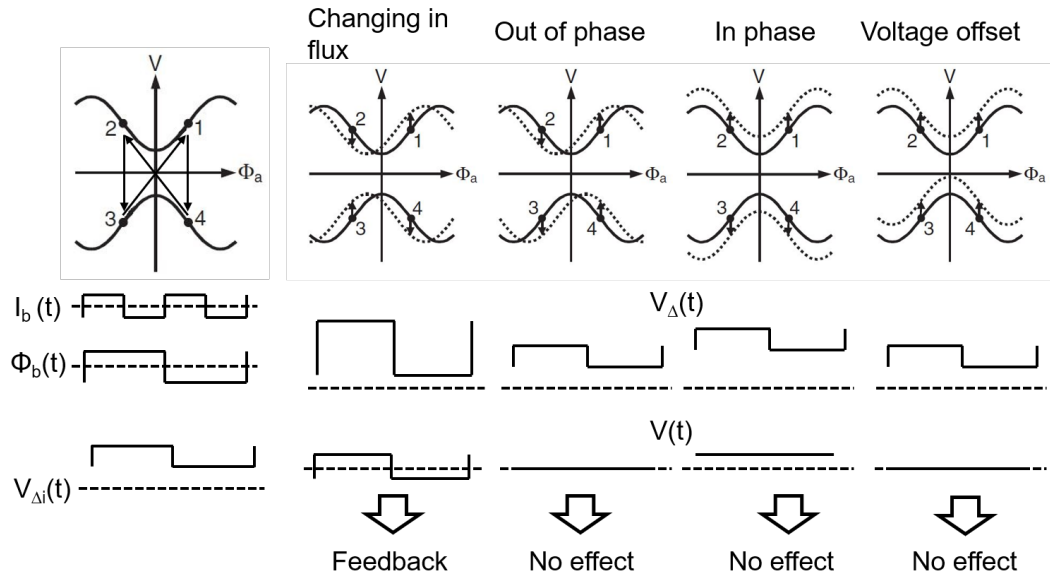
Figure 5.3: The DFLL lock theory based on the voltage level. The current bias I_b has twice the frequency as flux modulation Φ_b. By osculating between 2, 3 and 1, 4, the voltage difference between each point sets $V_{\Delta i}(t)$ could be calculated during the scanning period. While locking, the real time voltage difference $V_{\Delta}(t)$ will be compared and then produce a signal with same frequency as modulation signal.

5.4 Algorithm

A key advantage of using an FPGA is that software algorithms can be implemented and easily reprogrammed. Multiple algorithms have been developed based on the theories mentioned above, including the traditional current bias method. The parameters of DFLL can be easily changed through the user interface in order to optimize the sensitivities and noise for both HTS and LTS sensors with various dynamic ranges. Below is an example of a program being tested in our experimental setup.

Algorithm 1 (H) *Algorithm for DFLL*

Input: *ADC signal x*

Output: *DAC signal y, current bias I and digital output z*

1: **while** *ScanState* **do**

2:　　$I \leftarrow$ *periodic wave*

3:　　$y \leftarrow$ *periodic wave at each I*

4:　　**for** *each y and I* **do**

5:　　　　$PP_y(I)$*gets peak to peak y respond at I*

6:　　　　**if** $PP_y > PP_{max}$ **then**

7:　　　　　　$point_x(y, I) \leftarrow x$ *of optimal operating points*

8:　　　　**end if**

9:　　**end for**

10: **end while**

11:

12: **while** *LockState* **do**

52

13:     $y \leftarrow modulation\ signal$

14:     $I \leftarrow modulation\ signal\ with\ higher\ frequency$

15:     $\Delta y = \int point_x(y_o, I) - x\,dx$

16:     **if** $y \neq 0$ **then**

17:         $update\ y, z\ with\ ratio \times \Delta y$

18:     **end if**

19: **end while**

In this particular algorithm, the user modifiable parameters include both real time control and preset variables. Users can change the period, range, and gap of both the current bias and the magnetic field while scanning the SQUID. In the lock state, modulation frequency can be modified to fit different types of sensors and electronic system. The delay time has been pre-designed for the system we are using, but it can be changed depending on the frequency, cryosystem, and the sensor itself. The integration period and gains are also adjustable to provide the most sensitive and stable result. The functions and conditions which determine the optimal working points are the most important preset components that keep the SQUIDs working at the most preferable location.

During the scan state, the program will estimate the amplitude V_{PP} of the SQUID modulation to determine the best current bias range. This voltage information is stored in the FPGA for further possible analysis. Fig. 5.10 shows some of the data calculated during the scanning period. The red cross points are the possible working points determined by the adjustable functions and conditions. One way to estimate the points is by simply using the points that have highest slope in each period. Additional weighted conditions

can be added, including the linearity range, noise, and preferable voltage range, which will be demonstrated in the simulation and testing sections below. The working points are calculated during each period and stored in the FPGA for further data process and control, such as flux jumping and counting. The selection of these working points can also be conditioned into a preferable dynamic range. For example, the default pick will be in the middle of the DAC voltage range. However, if a change is expected in one direction of the external magnetic field, the modulation points could be conditioned to the other side in order to provide a larger dynamic range before it hits the boundary. The flux quanta Φ_0 is also estimated by averaging each period. The estimation can be done in two different ways, one is by subtracting between different local maximum or minimum points on each curve, the other one is by subtracting the optimal point determined during scanning period with the optimal function that enforces the working points at the middle voltage level.
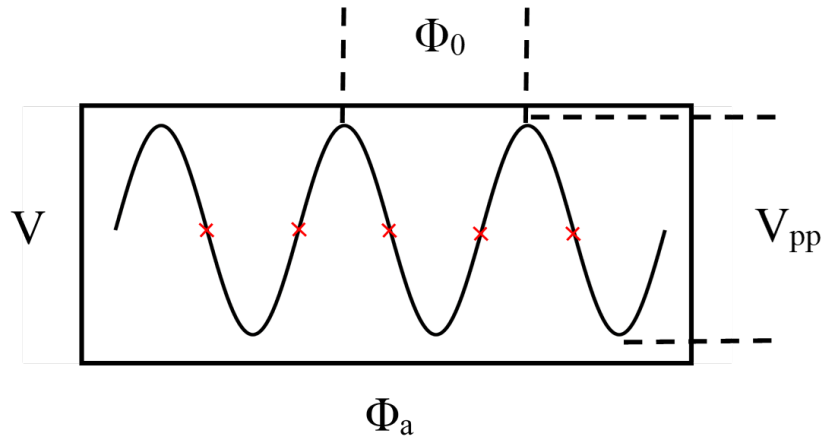
Figure 5.4: Information that is calculated during scanning period. During the scan period, both the voltage amplitude V_{PP} and flux quanta Φ_0 are estimated. The red points, which indicate the preferred working points, are calculated by the preset function for each period.

5.5 Simulation

We simulated our algorithm using a second FPGA system configured to mimic a real SQUID. In order to do this, we digitized real SQUID data from a previous transport measurement. The original SQUID data shown below in Fig. 2 is obtained from a typical YBCO SQUID fabricated in our lab [62]. The second FPGA system acts as a lookup table using the SQUID data with respect to both the input magnetic field signal and current bias. The virtual gain of this digital SQUID is set to 100, which brings the output to around the 100 mV level. This Digital SQUID behaves like a combination of the real SQUID and the pre-amplifier. It is then connected to the DFLL system using a DAC. The maximum slew rate was tested with the simulated SQUID. The 10 MHz frequency was applied with short coaxial cables in order to maximize the slew rate. The SQUID transfer function was linearized by the electronic system during this simulation.
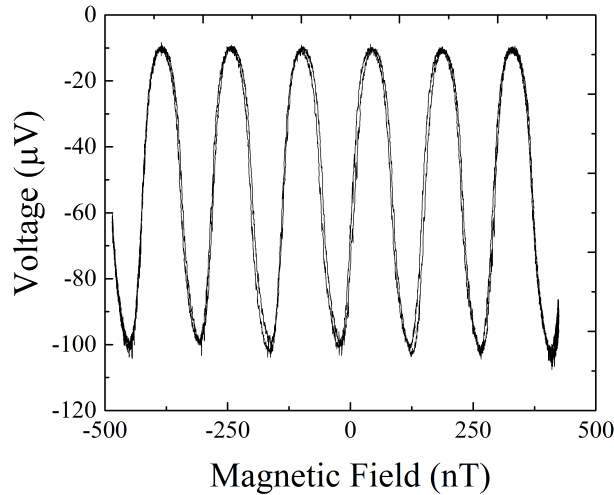
Figure 5.5: YBCO SQUID data used for simulation of the DFLL.

An additional simulation has been done to lock long junctions which were introduced in Chapter 2. Similar to the mimic SQUID, the original long junction data shown below Fig. 5.6 fabricated in our lab [51] is configured in the FPGA. The voltage output of this digital long junction has the exact same range as the real data, about 160 mV. Distinct from the SQUID FLL algorithm, the algorithm was modified to pick the working points in the linear regions that are closer to the peak point with relatively high sensitivity. This returns a magnetic field modulation amplitude of about 60 µT. The points which are closer to the peak are preferable for providing the smallest modulation amplitude possible, maintaining a relatively high sensitivity. In reality, higher magnetic field jumping might increase the settling time or ringing effect in feedback coil. This will decrease the modulation frequency to lock the long junction and reduce to a smaller slew rate. The algorithm has successfully linearized the long junction. However, for the real long junction test, the delay time has to be set for longer and the modulation frequency needed to be adjusted depending on the test system.

Due to this reasoning, current bias modulation has been applied to the simulated long junction array on one side of the V-B curve. Fig. 5.10 shows the locking points on the long junctions with bias reversal. Instead of frequency detection, the long junction array will be locked on the voltage calculation previously described. The range between each voltage response point will be integrated after subtracting a constant voltage. The constant voltage is obtained by subtracting the same working points from the initial state during the scanning period. The system will only feed back a voltage to balance out the applied flux, rather than the modulation, to lock the long junction at a certain voltage value. This
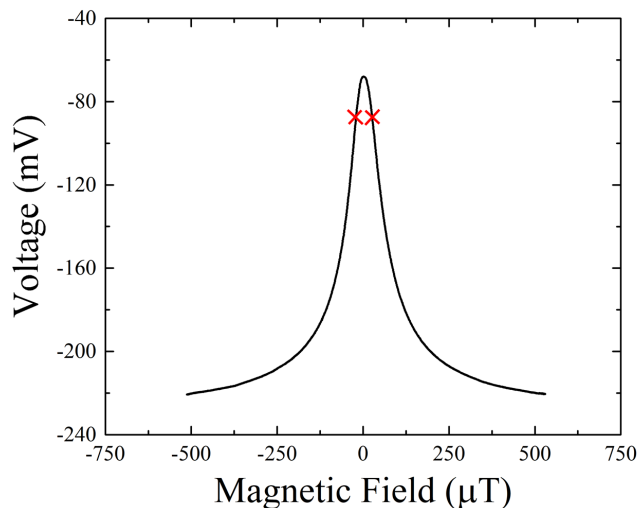
Figure 5.6: Long junction data used for simulation of DFLL. The red points indicated the working points of the long junctions. The working points are about 60 µT apart.

method can achieve a much higher frequency without considering the settling time or any other effects in the pick-up coil. Any out-of phase fluctuation noise from the current or voltage offset noise will not effect this system. However, considering the in-phase current and normal resistance fluctuation, this system can not cancel the noise which will then be applied on the feedback signal.

5.6   SQUID Measurement

We tested our DFLL on a YBCO direct inject nanoslit-SQUID design developed in our laboratory. A more detailed description of its fabrication [62] and inductive properties [82] are introduced by Cho *et al.* The configuration of this test consisted of a hexagonal loop with 300 μm height directly coupled to the nano-slit SQUID serving as a pick-up
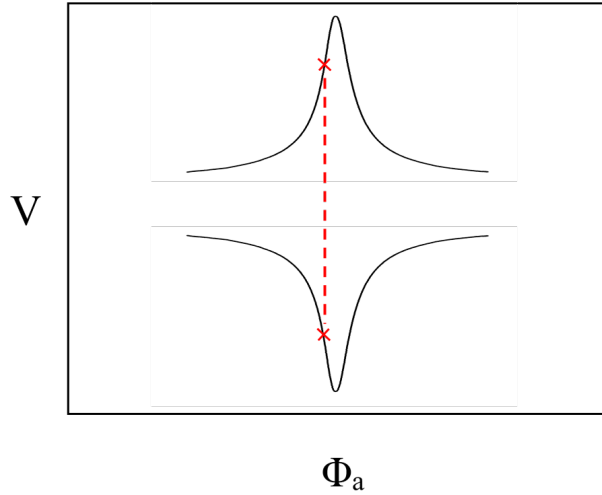
Figure 5.7: Current bias reversal for long junction. The top and bottom curve is the long junction transfer function at two different bias level. the red points indicates the working point in transfer function with two different bias current. The voltage difference in between will be used to lock the junction at these two working point.
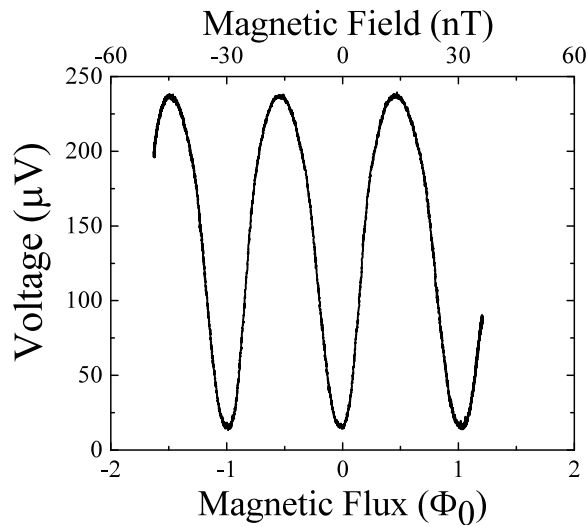
Figure 5.8: Voltage as a function of the magnetic flux and field for a YBCO direct inject nanoslit SQUID measured at 20 K.

loop, similar to the hexagonal SQUID that has been motioned in chapter 3. Using this configuration/set-up, the superconducting current induced from the magnetic flux in the pick-up loop directly couples into the SQUID and significantly enhances sensitivity [60]. An additional hexagonal loop was patterned around the pick-up loop for use as both a modulation and feedback coil. The on-chip coupling between the feedback coil and the pick up loop was about 40-50 pH. The junctions had a critical current of 5 μA at 20 K with a resistance of 4.2 Ω. The voltage response with respect to the magnetic field of the sensor operated around 20 K is shown in Fig. 5.8.

The complete digital system was connected to the SQUID and verified using the described algorithm to perform a scan of the data in order to obtain the properties of the SQUID sensor. Simultaneous with the scan, the FPGA estimates and records the SQUID oscillation period Φ_0, as well as the slopes, linearity, noise, and SQUID modulation amplitudes of the SQUID curve. Optimal working points are then calculated from this data for each period. Multiple algorithms have been tested for the determination of optimal points. In this example, we used a formula containing user-adjustable weights applied to the previously listed parameters in order to calculate a score for each point. In this calculation, higher scores indicate points with a steep slope, high linearity, low noise, and a large range of linearity. From this, the optimal points are those with a relatively high score within each period. These points are stored in the FPGA for further reference and operation. From these recorded optimal points, the two with the best score and the closest magnetic flux will be chosen for locking. A feature of these chosen points is that they do not necessarily have to be at same voltage level nor be half flux quanta apart, but the same

voltage and the same period are preferred by the algorithm. However, these conditions can be optionally enforced, a setting controlled by the user. After completion, the DFLL switches into locked mode, where the FPGA operates with separated working points. For this experiment, the modulation frequency of the system was set to 10 kHz because of our cryostat. It is not wired for higher speed operation. However, for other high frequency systems with high speed coax, the frequency can be easily modified through the FPGA, up to 10 MHz for each SQUID for optimized results. External magnetic field was applied to the SQUID in order to confirm the proper functioning of the whole system. The output with respect to the external magnetic flux is shown in Fig. 5.9. There, the SQUID transfer function has been linearized with respect to the external magnetic flux.
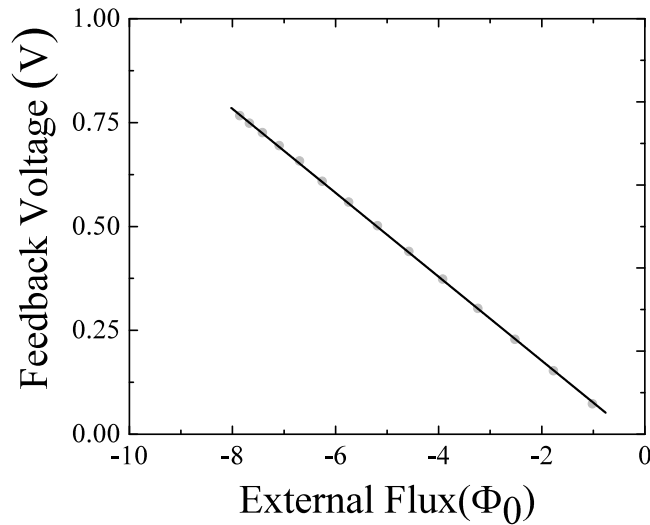
Figure 5.9: Output voltage of the digital feedback control system with respect to externally applied magnetic field. The grey dots represent the feedback voltage applied on the feedback coil. A linear regression shown above as a black line has been well fitted on the transfer function with adjusted R^2 equal to 99.982%.

60

5.7 Dynamic range

To overcome the limitations of the DAC while maintaining the sensitivity of the SQUID, boundaries were set for the feedback signal in the DAC. The DFLL will continue in locked mode until hitting the boundary [83]. As shown in Fig. 5.10, when the DAC output signal reached its predefined boundary, it was programmed to jump the operating point back by several corresponding flux quanta and to re-lock the SQUID. The jumper count and estimated flux quanta are stored in FPGA to provide an output proportional to the external magnetic field. Fig. 5.11 shows the feedback voltage and the digital output with respect to the magnetic field. The original digital data representing flux quanta is stored in a logic vector with a maximum of 32 bits. This can be easily expended to a greater capacity for even larger dynamic ranges. The small shifts on the digital output occur when a flux jump has been accomplished. The shifted values come from the difference between the flux quanta calculated from the scan stage and the actual flux jumped, Φ_{actual}. In this test, the FPGA controls the feedback voltage, causing it to jump back by an n value of calculated flux quanta when it reaches the predefined boundary. In our experiment, n = 2. After the jump, the DFLL will then lock the SQUID back to the optimal points on the current period.

Further DSP was performed in order to remove the digital output shift, shown in Fig. 5.12, which then completely linearized the transfer function of the SQUID, despite the inclusion of the flux jumps.
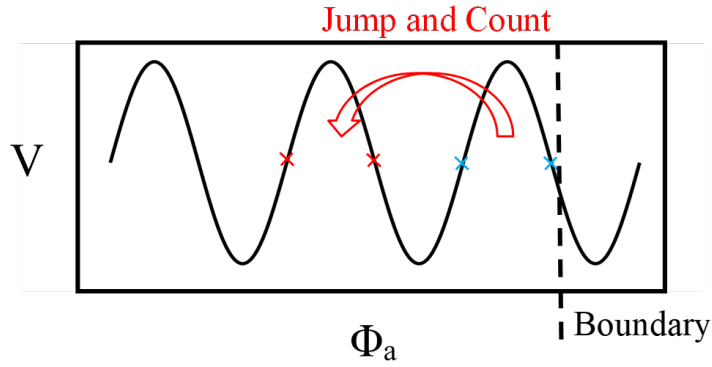
Figure 5.10: Demonstration of how combination of flux jumping, counting and re-locking works. Assuming the SQUID is locked at the blue points. When hitting the preset boundary, the working point will be jumped back to the red points and keep locking. This jump is achieve by using the estimated flux quanta and the stored working points from the scan period. The jumping amount will be counted and stored for further data analysis.
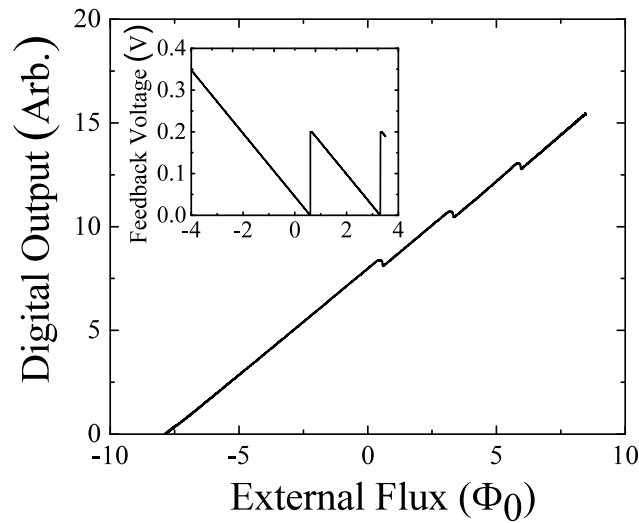
Figure 5.11: Digital readout with respect to applied magnetic flux. The shift on the digital output indicates the flux difference $\Delta\Phi = n\Phi_{0,est} - \Phi_{actual}$. The inset shows the feedback voltage versus the external magnetic flux applied. The voltage jump on the inset graph indicates the actual flux jump Φ_{actual} driven by the feedback coil.
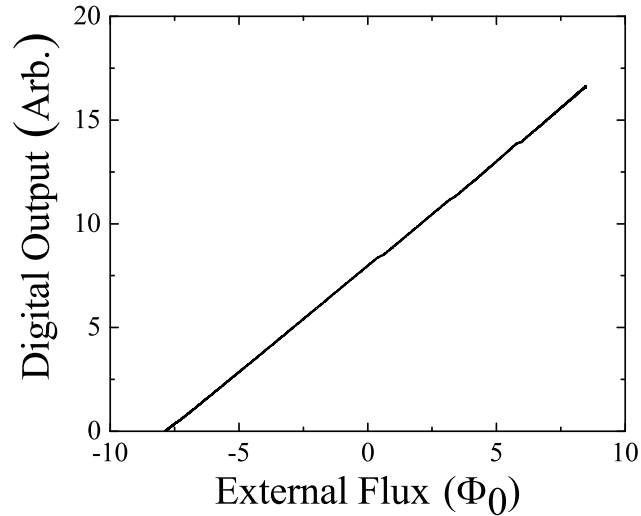
Figure 5.12: Digital output of the FPGA after applying additional data processing on the flux jumping and re-locking signal. The error between estimated flux and real flux can be determined and removed to produce a much linear transfer fucntion.

In the case of a high-T_C SQUID with planer Josephson Junctions, this method enables a wide dynamic range only limited by the SQUID junction's Fraunhofer pattern. When the external flux reaches the first minimum on the junction's Fraunhofer pattern, the DFLL will be unable to continue locking the SQUID as the voltage modulation will be too small. Fig. 5.13 below shows a range test that goes up to 80 flux quantum in total. In this experiment, our DFLL can lock up to at least 600 flux quantum within this YBCO SQUID limitation. This method may not be applicable to a tightly coupled input coil connected to a resonant circuit because ringing could create an interference that degrades the device performance.
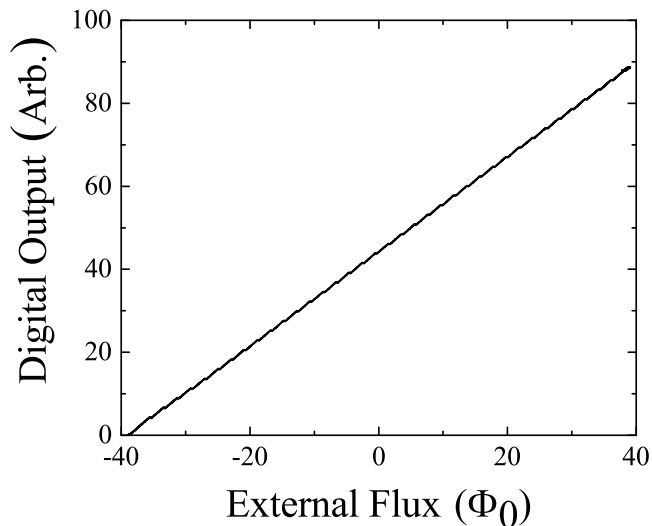
Figure 5.13: Digital output of FPGA for applied flux range from -40 Φ_0 to 40 Φ_0 with flux jumping and relocking.

5.8 Conclusion

The digital feedback system is easier to control and modify. The full scan provides detailed information about the particular SQUID sensor. In this system, optimal points can be selected and stored in the FPGA based on each user's requirements. Differing from the analog FLL locked points, these optimal points are solely focused on maximizing the slope and the linearity of the SQUID function in order to reduce the noise of the whole system. As we have demonstrated, the working points are not required to be at the same voltage level nor at the same current bias level in order to make this measurement. This quality provides a dynamic range only limited by SQUID sensor itself. Finally, changing various parameters while the system is in operation is much easier than before. Parameters, such as the sensitivity of the feedback system can be adjusted for changes in the speed of the magnetic field during testing. These control parameters can help to optimize the digital FLL

for a myriad of different sensors, each requiring distinct parameters such as SQUIDs [84] or Josephson arrays [51].

This new approach makes it easier to scale up the FPGA system to support a large number of sensors. Instead of having a multiple analog circuit, many different kinds of SQUID sensors can be integrated as a whole system, suitable for applications such as the operation of digital gradiometers and bio-medico scans. The individual signals from diverse SQUID sensors can be processed inside of the FPGA simultaneously during parallel processing.

Based on this technology, magnetic field mapping over various objects and areas with high sensitivity and large dynamic range are easily achievable feats. Other types of sensors, such as temperature and proximity sensors, can also be communicate with each other through the FPGA for more accurate results.

5.9   Acknowledgement

Chapter 6

Conclusions

This dissertation describes the result of research in high temperature superconducting magnetometers and the corresponding electronic control systems. Superconducting magnetometers with high sensitivity to magnetic flux are widely used in a variety of applications [1–15]. Most commercial superconductor devices are fabricated with LTS. With the rapid development of FHB technology, Josephson junctions made from YBCO can be fabricated on much smaller scales [26]. The electronic properties in the junction barriers are now controllable. Similarly, high performance devices can be developed with HTS that operate at much higher temperatures. The rise in temperature reduces the cost of operating sensors at liquid helium temperature. The higher temperature also reduces the distance between the sensors and objects. Since the magnetic field decreases proportionally to distance cubed, a closer distance could signify an increase in the resolution of the detection. Varieties of HTS sensors with different electronic properties and behaviors have been designed and tested for these applications with distinct requirements. More and more sensors are

combined into one system to provide optimal solutions. The traditional FLL electronics, which mainly focus on controlling LTS SQUIDs, have to be modified in order to operate HTS SQUIDs. The components may need to be switched depending on the sensors' electronic properties. A new scale-able electronics system with adjustable parameters that can simultaneously processes multiple sensors can meet the new demands.

Presented here is a summary of work following the FHB technology. The studies start from FHB YBCO junctions and then go to YBCO SQUID magnetometers and SQUID arrays, followed by the further development of a control system for these devices. The YBCO FHB Josephson junctions with different widths were first studied. The wider junctions, also known as the long junctions, provide a much more linear range on the voltage response with respect to magnetic field with a higher sensitivity. These long junctions are then made into arrays in order to enlarge the dynamic range and the voltage response. These devices can be operated in an unshielded environment with an impedance match to a variety of electronics. YBCO direct inject SQUIDs with different designs were then investigated, providing a much higher sensitivity to magnetic flux. A set of SQUIDs with rectangular pick-up loops which can operate above 50 K were designed for further SQUID imaging. When compared to the image from SQUID arrays with rectangular or hexagonal pick-up loops, the simulations show that the rotation of rectangular SQUID sets can reconstruct an image with better resolution using the same area of the pick-up loops. SQUID arrays were also studied for the purpose of improving the dynamic range, bandwidth, and linearity of SQUID magnetometers. The geometries and current distributions were simulated to have a deeper understanding of the electronic properties. The current distribution indicated

the size limitation for future devices with certain geometries. The current density with respect to effective area was fitted to the V-B characteristics of differently sized SQUID arrays. Multiple solutions have been found to have non-uniformly distributed current. An electronic control system is then developed based on FLL theory to control several devices, mainly SQUID magnetometers, with different electronic properties and behaviors. The dynamic range of the SQUID is enlarged to the limit of junction's Fraunhofer pattern itself by combining the flux lock and flux jumping and counting. The system can now be scaled up easily in order to achieve multi-sensor control and parallel processing.

Further optimization of these magnetometer devices are suggested to enhance performance. The interference effect in SQUID arrays requires further investigation because the current distribution in the devices is still an open question. Magnetic field mapping and imaging performed by electronic control systems using parallel processing of multiple sensors are an interesting direction for future studies.

Bibliography

[1] John Clarke and Alex I Braginski. *The SQUID handbook: Applications of SQUIDs and SQUID systems*. John Wiley & Sons, 2006.

[2] Harold Weinstock. *SQUID sensors: fundamentals, fabrication and applications*, volume 329. Springer Science & Business Media, 2012.

[3] Boris Chesca, Daniel John, Matthew Kemp, Jeffrey Brown, and Christopher Mellor. Parallel array of yba2cu3o7- δ superconducting josephson vortex-flow transistors with high current gains. *Applied Physics Letters*, 103(9):092601, 2013.

[4] Igor V Vernik, Dmitri E Kirichenko, Vladimir V Dotsenko, Robert Miller, Robert J Webber, Pavel Shevchenko, Andrei Talalaevskii, Deepnarayan Gupta, and Oleg A Mukhanov. Cryocooled wideband digital channelizing radio-frequency receiver based on low-pass adc. *Superconductor Science and Technology*, 20(11):S323, 2007.

[5] Igor V Vernik, Vitaly V Bol'ginov, Sergey V Bakurskiy, Alexander A Golubov, Mikhail Yu Kupriyanov, Valery V Ryazanov, and Oleg A Mukhanov. Magnetic josephson junctions with superconducting interlayer for cryogenic memory. *IEEE transactions on applied superconductivity*, 23(3):1701208–1701208, 2012.

[6] Victor K Kornev, Igor I Soloviev, Alexey V Sharafiev, Nikolay V Klenov, and Oleg A Mukhanov. Active electrically small antenna based on superconducting quantum array. *IEEE transactions on applied superconductivity*, 23(3):1800405–1800405, 2012.

[7] Susan Berggren, G Prokopenko, P Longhini, A Palacios, Oleg A Mukhanov, A Leese De Escobar, BJ Taylor, MC De Andrade, M Nisenoff, Robert L Fagaly, et al. Development of 2-d bi-squid arrays with high linearity. *IEEE transactions on applied superconductivity*, 23(3):1400208–1400208, 2013.

[8] J Du, AD Hellicar, Li Li, SM Hanham, N Nikolic, JC Macfarlane, and KE Leslie. Terahertz imaging using a high-tc superconducting josephson junction detector. *Superconductor Science and Technology*, 21(12):125025, 2008.

[9] EE Mitchell, KE Hannam, J Lazar, KE Leslie, CJ Lewis, A Grancea, ST Keenan, SKH Lam, and CP Foley. 2d sqif arrays using 20 000 ybco high r n josephson junctions. *Superconductor Science and Technology*, 29(6):06LT01, 2016.

[10] Catherine P Foley, KE Leslie, R Binks, Christoper Lewis, Wayne Murray, GJ Sloggett, S Lam, B Sankrithyan, N Savvides, A Katzaros, et al. Field trials using hts squid magnetometers for ground-based and airborne geophysical applications. *IEEE transactions on applied superconductivity*, 9(2):3786–3792, 1999.

[11] Roland Fischer, Filomena Longo, Peter Nielsen, Rainer Engelhardt, Robert C Hider, and Antonio Piga. Monitoring long-term efficacy of iron chelation therapy by deferiprone and desferrioxamine in patients with β-thalassaemia major: application of squid biomagnetic liver susceptometry. *British journal of haematology*, 121(6):938–948, 2003.

[12] MI Faley, U Poppe, RE Dunin Borkowski, M Schiek, F Boers, H Chocholacs, J Dammers, E Eich, NJ Shah, AB Ermakov, et al. Magnetoencephalography using a multilayer hightc dc squid magnetometer. *Physics Procedia*, 36:66–71, 2012.

[13] Yu Pei Ma and John P Wikswo. Squid magnetometers for depth-selective, oriented eddy current imaging. In *Review of Progress in Quantitative Nondestructive Evaluation*, pages 1067–1074. Springer, 1998.

[14] Benjamin P Weiss, Eduardo A Lima, Luis E Fong, and Franz J Baudenbacher. Paleomagnetic analysis using squid microscopy. *Journal of Geophysical Research: Solid Earth*, 112(B9), 2007.

[15] MA Dobbs, M Lueker, KA Aird, AN Bender, BA Benson, LE Bleem, JE Carlstrom, CL Chang, H-M Cho, J Clarke, et al. Frequency multiplexed superconducting quantum interference device readout of large bolometer arrays for cosmic microwave background measurements. *Review of Scientific Instruments*, 83(7):073113, 2012.

[16] Mark D Ainslie. *Transport AC loss in high temperature superconducting coils*. PhD thesis, University of Cambridge, 2012.

[17] JM Valles Jr, AE White, KT Short, RC Dynes, JP Garno, AFJ Levi, M Anzlowar, and K Baldwin. Ion-beam-induced metal-insulator transition in y ba 2 cu 3 o 7- δ: A mobility edge. *Physical Review B*, 39(16):11599, 1989.

[18] Theodore Van Duzer and Charles William Turner. Principles of superconductive devices and circuits. 1981.

[19] Dietmar Drung. High-tc and low-tc dc squid electronics. *Superconductor Science and Technology*, 16(12):1320, 2003.

[20] O Dossel, B David, M Fuchs, WH Kullmann, and K Ludeke. A modular low noise 7-channel squid-magnetometer. *IEEE transactions on magnetics*, 27(2):2797–2800, 1991.

[21] Ethan Y Cho, Yuchao W Zhou, Mikhail M Khapaev, and Shane A Cybart. Investigation of arrays of two-dimensional high-t_c squids for optimization of electrical properties. *IEEE Transactions on Applied Superconductivity*, 29(5):1–4, 2019.

[22] Maw-Kuen Wu, Jo R Ashburn, ClJ Torng, Ph H Hor, Rl L Meng, Lo Gao, Z Jo Huang, YQ Wang, and aCW Chu. Superconductivity at 93 k in a new mixed-phase y-ba-cu-o compound system at ambient pressure. *Physical review letters*, 58(9):908, 1987.

[23] T Scherer, P Marienhoff, R Herwig, M Neuhaus, and W Jutzi. Anisotropy on the a, b-plane of c-axis orientated almost twin-free ybco films on ndgao3. *Physica C: Superconductivity*, 197(1-2):79–83, 1992.

[24] Alice E White, KT Short, RC Dynes, AFJ Levi, M Anzlowar, KW Baldwin, PA Polakos, TA Fulton, and LN Dunkleberger. Controllable reduction of critical currents in yba2cu3o7- δ films. *Applied physics letters*, 53(11):1010–1012, 1988.

[25] BW Ward, John A Notte, and NP Economou. Helium ion microscope: A new tool for nanoscale microscopy and metrology. *Journal of Vacuum Science & Technology B: Microelectronics and Nanometer Structures Processing, Measurement, and Phenomena*, 24(6):2871–2874, 2006.

[26] Shane A Cybart, EY Cho, TJ Wong, Björn H Wehlin, Meng K Ma, Chuong Huynh, and RC Dynes. Nano josephson superconducting tunnel junctions in yba 2 cu 3 o 7–δ directly patterned with a focused helium ion beam. *Nature nanotechnology*, 10(7):598, 2015.

[27] Brian Josephson. Possible new effect in superconducting tunneling. *Phys. Lett.*, 1:251–253, 1962.

[28] Antonio Barone and Gianfranco Paterno. *Physics and applications of the Josephson effect*. Wiley, 1982.

[29] WC Stewart. Current-voltage characteristics of josephson junctions. *Applied Physics Letters*, 12(8):277–280, 1968.

[30] DE McCumber. Effect of ac impedance on dc voltage-current characteristics of superconductor weak-link junctions. *Journal of Applied Physics*, 39(7):3113–3118, 1968.

[31] RC Jaklevic, John Lambe, AH Silver, and JE Mercereau. Quantum interference effects in josephson tunneling. *Physical Review Letters*, 12(7):159, 1964.

[32] D Drung, H Matz, and H Koch. A 5-mhz bandwidth squid magnetometer with additional positive feedback. *Review of scientific instruments*, 66(4):3008–3015, 1995.

[33] E Dantsker, S Tanaka, P-Å Nilsson, R Kleiner, and John Clarke. Reduction of 1/f noise in high-t c dc superconducting quantum interference devices cooled in an ambient magnetic field. *Applied physics letters*, 69(26):4099–4101, 1996.

[34] J Beyer, D Drung, F Ludwig, and Th Schurig. Linearity of sensitive yba 2 cu 3 o 7-x dc superconducting quantum interference device magnetometers. *Journal of applied physics*, 86(6):3382–3386, 1999.

[35] RL Forgacs and A Warnick. Digital-analog magnetometer utilizing superconducting sensor. *Review of Scientific Instruments*, 38(2):214–220, 1967.

[36] John Clarke, Wolfgang M Goubau, and Mark B Ketchen. Tunnel junction dc squid: fabrication, operation, and performance. *Journal of Low Temperature Physics*, 25(1-2):99–144, 1976.

[37] D Koelle, R Kleiner, F Ludwig, E Dantsker, and John Clarke. High-transition-temperature superconducting quantum interference devices. *Reviews of Modern Physics*, 71(3):631, 1999.

[38] Michael B Simmonds and Robin P Giffard. Apparatus for reducing low frequency noise in dc biased squids, June 21 1983. US Patent 4,389,612.

[39] Roger H Koch, John Clarke, WM Goubau, John M Martinis, CM Pegrum, and Dale J Van Harlingen. Flicker (1/f) noise in tunnel junction dc squids. *Journal of low temperature physics*, 51(1-2):207–224, 1983.

[40] V Foglietti, WJ Gallagher, MB Ketchen, AW Kleinsasser, RH Koch, SI Raider, and RL Sandstrom. Low-frequency noise in low 1/f noise dc squid's. *Applied physics letters*, 49(20):1393–1395, 1986.

[41] V Foglietti, W Gallagher, and R Koch. A novel modulation technique for 1/f noise reduction in dc squids. *IEEE Transactions on Magnetics*, 23(2):1150–1153, 1987.

[42] S Kuriki, M Matsuda, and A Matachi. Effects of alternating bias current on the low-frequency noise in dc squids. *Journal of applied physics*, 64(1):239–241, 1988.

[43] CS Owen and DJ Scalapino. Vortex structure and critical currents in josephson junctions. *Physical Review*, 164(2):538, 1967.

[44] Tsutomu Yamashita and Yutaka Onodera. Magnetic-field dependence of josephson current influenced by self-field. *Journal of Applied Physics*, 38(9):3523–3525, 1967.

[45] YM Zhang, D Winkler, and T Claeson. Detection of mm and submm wave radiation from soliton and flux-flow modes in a long josephson junction. *IEEE transactions on applied superconductivity*, 3(1):2520–2523, 1993.

[46] V Martin, M Lam Chok Sing, D Robbes, J Certenais, N Quellec, and D Crete. Magnetometry based on sharpened high t/sub c/gbj fraunhofer patterns. *IEEE transactions on applied superconductivity*, 7(2):3079–3082, 1997.

[47] Antonio Vettoliere, Carmine Granata, and Roberto Monaco. Long josephson junction in ultralow-noise magnetometer configuration. *IEEE Transactions on Magnetics*, 51(1):1–4, 2015.

[48] J Du, JY Lazar, SKH Lam, EE Mitchell, and CP Foley. Fabrication and characterisation of series ybco step-edge josephson junction arrays. *Superconductor Science and Technology*, 27(9):095005, 2014.

[49] Shane A Cybart, Steven M Anton, Stephen M Wu, John Clarke, and Robert C Dynes. Very large scale integration of nanopatterned yba2cu3o7- δ josephson junctions in a two-dimensional array. *Nano letters*, 9(10):3581–3585, 2009.

[50] Ethan Cho. *Focused Helium Beam Irradiated Josephson Junctions.* PhD thesis, UC San Diego, 2016.

[51] Jay C LeFebvre, Ethan Cho, Hao Li, Kevin Pratt, and Shane A Cybart. Series arrays of planar long josephson junctions for high dynamic range magnetic flux detection. *AIP Advances*, 9(10):105215, 2019.

[52] Riccardo Arpaia, Marco Arzeo, Shahid Nawaz, Sophie Charpentier, Floriana Lombardi, and Thilo Bauch. Ultra low noise yba2cu3o7- δ nano superconducting quantum interference devices implementing nanowires. *Applied Physics Letters*, 104(7):072603, 2014.

[53] Tobias Schwarz, Roman Wölbing, Christopher F Reiche, Benedikt Müller, Maria-José Martínez-Pérez, Thomas Mühl, Bernd Büchner, Reinhold Kleiner, and Dieter Koelle. Low-noise yba 2 cu 3 o 7 nano-squids for performing magnetization-reversal measurements on magnetic nanoparticles. *Physical Review Applied*, 3(4):044011, 2015.

[54] Denis Vasyukov, Yonathan Anahory, Lior Embon, Dorri Halbertal, Jo Cuppens, Lior Neeman, Amit Finkler, Yehonathan Segev, Yuri Myasoedov, Michael L Rappaport, et al. A scanning superconducting quantum interference device with single electron spin sensitivity. *Nature nanotechnology*, 8(9):639–644, 2013.

[55] R Arpaia, M Arzeo, R Baghdadi, E Trabaldo, F Lombardi, and T Bauch. Improved noise performance of ultrathin ybco dayem bridge nanosquids. *Superconductor Science and Technology*, 30(1):014008, 2016.

[56] Lei Chen, Hao Wang, Xiaoyu Liu, Long Wu, and Zhen Wang. A high-performance nb nano-superconducting quantum interference device with a three-dimensional structure. *Nano letters*, 16(12):7726–7730, 2016.

[57] M Schmelz, A Vettoliere, V Zakosarenko, N De Leo, M Fretto, R Stolz, and C Granata. 3d nanosquid based on tunnel nano-junctions with an energy sensitivity of 1.3 h at 4.2 k. *Applied Physics Letters*, 111(3):032604, 2017.

[58] MB Ketchen and JM Jaycox. Ultra-low-noise tunnel junction dc squid with a tightly coupled planar input coil. *Applied Physics Letters*, 40(8):736–738, 1982.

[59] Mark B Ketchen, Wolfgang M Goubau, John Clarke, and Gordon B Donaldson. Superconducting thin-film gradiometer. *Journal of Applied Physics*, 49(7):4111–4116, 1978.

[60] D Drung, R Cantor, M Peters, HJ Scheer, and HAPF Koch. Low-noise high-speed dc superconducting quantum interference device magnetometer with simplified feedback electronics. *Applied physics letters*, 57(4):406–408, 1990.

[61] D Koelle, AH Miklich, F Ludwig, E Dantsker, DT Nemeth, and John Clarke. dc squid magnetometers from single layers of yba2cu3o7- x. *Applied physics letters*, 63(16):2271–2273, 1993.

[62] Ethan Y Cho, Hao Li, Jay C LeFebvre, Yuchao W Zhou, RC Dynes, and Shane A Cybart. Direct-coupled micro-magnetometer with y-ba-cu-o nano-slit squid fabricated with a focused helium ion beam. *Applied physics letters*, 113(16):162602, 2018.

[63] MM Khapaev, M Yu Kupriyanov, E Goldobin, and M Siegel. Current distribution simulation for superconducting multi-layered structures. *Superconductor Science and Technology*, 16(1):24, 2002.

[64] MM Khapaev and M Yu Kupriyanov. Inductance extraction of superconductor structures with internal current sources. *Superconductor Science and Technology*, 28(5):055013, 2015.

[65] Victor K Kornev, Alexey V Sharafiev, Igor I Soloviev, Nikolay V Kolotinskiy, Vitaly A Scripka, and Oleg A Mukhanov. Superconducting quantum arrays. *IEEE Transactions on Applied Superconductivity*, 24(4):1–6, 2014.

[66] S Ouanani, J Kermorvant, C Ulysse, M Malnou, Y Lemaître, B Marcilhac, C Feuillet-Palma, N Bergeal, D Crété, and J Lesueur. High-tc superconducting quantum interference filters (sqifs) made by ion irradiation. *Superconductor science and technology*, 29(9):094002, 2016.

[67] Oleg V Snigirev, Maxim L Chukharkin, Alexey S Kalabukhov, Michael A Tarasov, Anatoly A Deleniv, Oleg A Mukhanov, and Dag Winkler. Superconducting quantum interference filters as rf amplifiers. *IEEE transactions on applied superconductivity*, 17(2):718–721, 2007.

[68] J Oppenländer, Ch Häussler, and N Schopohl. N o n- ϕ 0- p e r i o d i c macroscopic quantum interference in one-dimensional parallel josephson junction arrays with unconventional grating structure. *Physical review B*, 63(2):024511, 2000.

[69] Dietmar Drung, Colmar Hinnrichs, and Henry-Jobes Barthelmess. Low-noise ultrahigh-speed dc squid readout electronics. *Superconductor Science and Technology*, 19(5):S235, 2006.

[70] Martin E Huber, Patricia A Neil, Robert G Benson, Deborah A Burns, AF Corey, Christopher S Flynn, Yevgeniya Kitaygorodskaya, Omid Massihzadeh, John M Martinis, and GC Hilton. Dc squid series array amplifiers with 120 mhz bandwidth (corrected). *IEEE Transactions on Applied Superconductivity*, 11(2):4048–4053, 2001.

[71] VK Kornev, II Soloviev, J Oppenlaender, Ch Haeussler, and N Schopohl. The oscillation linewidth and noise characteristics of a parallel superconducting quantum interference filter. *Superconductor Science and Technology*, 17(5):S406, 2004.

[72] EY Cho, Kirill Kouperine, Yuchao Zhuo, RC Dynes, and SA Cybart. The effects of annealing a 2-dimensional array of ion-irradiated josephson junctions. *Superconductor Science and Technology*, 29(9):094004, 2016.

[73] Hirokuni Oda, Jun Kawai, Masakazu Miyamoto, Isoji Miyagi, Masahiko Sato, Atsushi Noguchi, Yuhji Yamamoto, Jun-ichi Fujihira, Nobuyoshi Natsuhara, Yoshiyasu Aramaki, et al. Scanning squid microscope system for geological samples: system integration and initial evaluation. *Earth, Planets and Space*, 68(1):179, 2016.

[74] Vadim S Zotev, Andrei N Matlashov, Petr L Volegov, Igor M Savukov, Michelle A Espy, John C Mosher, John J Gomez, and Robert H Kraus Jr. Microtesla mri of the human brain combined with meg. *Journal of Magnetic Resonance*, 194(1):115–120, 2008.

[75] Frederick Wellstood, C Heiden, and John Clarke. Integrated dc squid magnetometer with a high slew rate. *Review of scientific instruments*, 55(6):952–957, 1984.

[76] Robin P Giffard. Flux locked loop, January 18 1977. US Patent 4,004,217.

[77] Daisuke Oyama, Koichiro Kobayashi, Masahito Yoshizawa, and Yoshinori Uchikawa. Development of digital fll system for squid using double counter method. *IEEE transactions on magnetics*, 42(10):3539–3541, 2006.

[78] C Ludwig, C Kessler, AJ Steinforc, and W Ludwig. Versatile high performance digital squid electronics. *IEEE transactions on applied superconductivity*, 11(1):1122–1125, 2001.

[79] Stephen D Brown, Robert J Francis, Jonathan Rose, and Zvonko G Vranesic. *Field-programmable gate arrays*, volume 180. Springer Science & Business Media, 2012.

[80] Stephen M Trimberger. *Field-programmable gate array technology*. Springer Science & Business Media, 2012.

[81] David F Hoeschele. *Analog-to-digital and digital-to-analog conversion techniques*, volume 968. Wiley New York, 1994.

[82] Hao Li, Ethan Y Cho, Han Cai, Yan-Ting Wang, Stephen J McCoy, and Shane A Cybart. Inductance investigation of yba 2 cu 3 o 7- δ nano-slit squids fabricated with a focused helium ion beam. *IEEE Transactions on Applied Superconductivity*, 29(5):1–4, 2019.

[83] M v Kreutzbruck, A Theiss, M Mück, and C Heiden. Compensation electronics for larger dynamic range of a squid based nondestructive evaluation system. *Review of scientific instruments*, 70(9):3714–3718, 1999.

[84] Shane A Cybart, TN Dalichaouch, SM Wu, SM Anton, JA Drisko, JM Parker, BD Harteneck, and RC Dynes. Comparison of measurements and simulations of series-parallel incommensurate area superconducting quantum interference device arrays fabricated from yba2cu3o7- δ ion damage josephson junctions. *Journal of Applied Physics*, 112(6):063911, 2012.

[85] Yuchao W Zhou, Hao Li, Ethan Y Cho, Han Cai, Guy Covert, and Shane A Cybart. Electronic feedback system for superconducting quantum interference devices. *IEEE Transactions on Applied Superconductivity*, 30(7):1–5, 2020.

[86] Alice E White, KT Short, DC Jacobson, JM Poate, RC Dynes, PM Mankiewich, WJ Skocpol, RE Howard, M Anzlowar, KW Baldwin, et al. Ion-beam-induced destruction of superconducting phase coherence in yba 2 cu 3 o 7- δ. *Physical Review B*, 37(7):3755, 1988.

[87] EY Cho, MK Ma, Chuong Huynh, K Pratt, DN Paulson, VN Glyantsev, RC Dynes, and Shane A Cybart. Yba2cu3o7- δ superconducting quantum interference devices with metallic to insulating barriers written with a focused helium ion beam. *Applied physics letters*, 106(25):252601, 2015.